

Systematic infrared 2.5–5 μm spectroscopy of nearby ultraluminous infrared galaxies with AKARI

Masatoshi IMANISHI *

National Astronomical Observatory, 2-21-1, Osawa, Mitaka, Tokyo 181-8588, Japan
masa.imanishi@nao.ac.jp

Takao NAKAGAWA, Yoichi OHYAMA [†], Mai SHIRAHATA, Takehiko WADA

Institute of Space and Astronautical Science, Japan Aerospace Exploration Agency, 3-1-1 Yoshinodai, Sagamihara, Kanagawa 229-8510, Japan

Takashi ONAKA

Department of Astronomy, Graduate School of Science, University of Tokyo, Bunkyo-ku, Tokyo 113-0033, Japan

and

Nagisa OI [‡]

Department of Astronomy, School of Science, Graduate University for Advanced Studies, Mitaka, Tokyo 181-8588, Japan

(Received 2008 May 6; accepted 2008 0)

Abstract

We report on the results of systematic infrared 2.5–5 μm spectroscopy of 45 nearby ultraluminous infrared galaxies (ULIRGs) at $z < 0.3$ using the IRC infrared spectrograph onboard the AKARI satellite. This paper investigates whether the luminosities of these ULIRGs are dominated by starburst activity, or alternatively, whether optically elusive buried active galactic nuclei (AGNs) are energetically important. Our criteria include the strengths of the 3.3 μm polycyclic aromatic hydrocarbon (PAH) emission features and the optical depths of absorption features at 3.1 μm due to ice-covered dust grains and at 3.4 μm from bare carbonaceous dust grains. Because of the AKARI IRC's spectroscopic capability in the full 2.5–5 μm wavelength range, unaffected by Earth's atmosphere, we can apply this energy diagnostic method to ULIRGs at $z > 0.15$. We estimate the intrinsic luminosities of extended (several kpc), modestly obscured ($A_V < 15$ mag) starburst activity based on the observed 3.3 μm PAH emission luminosities measured in AKARI IRC slitless spectra, and confirm that such starbursts are energetically unimportant in nearby ULIRGs. In roughly half of the observed ULIRGs classified optically as non-Seyferts, we find signatures of luminous energy sources that produce no PAH emission and/or are more centrally concentrated than the surrounding dust. We interpret these energy sources as buried

AGNs. The fraction of ULIRGs with detectable buried AGN signatures is higher in ULIRGs classified optically as LINERs than HII-regions, and increases with increasing infrared luminosity. Our overall results support the scenario that luminous buried AGNs are important in many ULIRGs at $z < 0.3$ classified optically as non-Seyferts, and that the optical undetectability of such buried AGNs occurs merely because of a large amount of nuclear dust, which can make the sightline of even the lowest dust column density opaque to the ionizing radiation of the AGNs.

Key words: galaxies: active — galaxies: nuclei — galaxies: ISM — infrared: galaxies

1. Introduction

Ultraluminous infrared galaxies (ULIRGs) have large luminosities ($L > 10^{12}L_{\odot}$) that are radiated mostly as infrared dust emission (Sanders et al. 1988a; Sanders & Mirabel 1996). This means that very luminous energy sources ($L > 10^{12}L_{\odot}$) are present hidden behind dust, so that most of the energetic photons from these energy sources are once absorbed by the surrounding dust and the heated dust then emits strongly in the infrared. The ULIRG population dominates the bright end of the luminosity function in the local universe ($z < 0.3$) (Soifer et al. 1987). The contribution from ULIRGs to the total infrared radiation density increases rapidly with increasing redshift (Le Flocc’h et al. 2005) and becomes important at $z > 1.3$ (Perez-Gonzalez et al. 2005). Distinguishing whether the dust-obscured energy sources of ULIRGs are dominated by starburst activity (nuclear fusion inside stars), or whether active galactic nuclei (AGNs; active mass accretion onto compact supermassive black holes with $M > 10^7M_{\odot}$) are also energetically important, is closely related to unveiling the history of dust-obscured star formation and supermassive black hole growth in the universe.

Identifying the dust-obscured energy sources in ULIRGs is difficult because a large amount of molecular gas and dust is concentrated in the nuclear regions of ULIRGs (Downes & Solomon 1998; Imanishi et al. 2006b; Imanishi et al. 2007b), and can easily *bury* (= obscure in all directions) the putative AGNs because the emitting regions of AGNs are spatially very compact. Unlike AGNs obscured by torus-shaped dust, which are classified optically as Seyfert 2s, such *buried* AGNs are elusive to conventional optical spectroscopy (Maiolino et al. 2003), and thus very difficult to detect. However, quantitative determination of the energetic importance

* Department of Astronomy, School of Science, Graduate University for Advanced Studies, Mitaka, Tokyo 181-8588, Japan

† Present address: Institute of Astronomy and Astrophysics Academia Sinica, P.O. Box 23-141, Taipei 10617, Taiwan, R.O.C.

‡ National Astronomical Observatory, 2-21-1, Osawa, Mitaka, Tokyo 181-8588, Japan

of buried AGNs is indispensable in understanding the true nature of the ULIRG population.

To study such optically elusive buried AGNs in ULIRGs, observing them at wavelengths of low dust extinction is important. Infrared 3–4 μm (rest-frame) spectroscopy is one such wavelength. Dust extinction at 3–4 μm is as low as that at 5–13 μm (Lutz et al. 1996). More importantly, starburst and AGN emission are distinguishable from spectral shapes based on the following two arguments. (1) A normal starburst galaxy should always show large equivalent width polycyclic aromatic hydrocarbons (PAH) emission at rest-frame 3.3 μm , while an AGN shows a PAH-free continuum originating in AGN-heated hot dust emission (Moorwood 1986; Imanishi & Dudley 2000; Imanishi et al. 2006a). Hence, if the equivalent width of the 3.3 μm PAH emission is substantially smaller than that of starburst-dominated galaxies, then a significant contribution from an AGN to the observed 3–4 μm flux is the most natural explanation (Imanishi & Dudley 2000; Imanishi et al. 2001; Imanishi & Maloney 2003; Imanishi et al. 2006a; Imanishi 2006). (2) In a normal starburst, the stellar energy sources and dust are spatially well mixed (Figure 1a), while in a buried AGN, the energy source (= a compact mass accreting supermassive black hole) is more centrally concentrated than the surrounding dust (Figure 1b). In a normal starburst with mixed dust/source geometry, the optical depths of dust absorption features at 3.1 μm by ice-covered dust and at 3.4 μm by bare carbonaceous dust cannot exceed certain thresholds, but can be arbitrarily large in a buried AGN (Imanishi & Maloney 2003; Imanishi et al. 2006a). Therefore, detection of strong dust absorption features whose optical depths are substantially larger than the upper limits set by mixed dust/source geometry suggests the buried-AGN-like centrally concentrated energy source geometry (Imanishi & Maloney 2003; Imanishi et al. 2006a).

Infrared 3–4 μm slit spectroscopy of a large sample of nearby ULIRGs using infrared spectrographs attached to ground-based large telescopes was performed, and signatures of intrinsically luminous buried AGNs were found in a significant fraction of optically non-Seyfert ULIRGs (Imanishi & Dudley 2000; Imanishi et al. 2001; Imanishi & Maloney 2003; Imanishi et al. 2006a; Risaliti et al. 2006; Imanishi 2006; Imanishi et al. 2007b; Sani et al. 2008). However, the observed sample was restricted to $z < 0.15$ because above this redshift, a part of the above-mentioned spectral features pass beyond the Earth’s atmospheric window (L -band; 2.8–4.1 μm), making this 3–4 μm energy diagnostic method impossible. Because of the 2.5–5 μm spectroscopic capability of the IRC (Onaka et al. 2007; Ohyama et al. 2007), which was mounted onboard the AKARI satellite (Murakami et al. 2007) and thus unaffected by Earth’s atmosphere, we can now extend this successful approach to more distant ULIRGs at $z > 0.15$. As AKARI IRC spectroscopy from space is quite sensitive, given the lack of large background emission from Earth’s atmosphere, this extension to higher redshift is feasible in terms of sensitivity. Additionally, the AKARI IRC employs slitless spectroscopy, so that the bulk of the extended starburst emission in host galaxies ($>$ several kpc scale) is covered, unless it is extended more than $1 \times 1 \text{ arcmin}^2$ (Onaka et al. 2007). The observed 3.3 μm PAH emission luminosities in the

AKARI IRC spectra can thus be used to roughly estimate the intrinsic luminosities of modestly obscured ($A_V < 15$ mag) extended starbursts in the ULIRG host galaxies, which is impossible with ground-based spectroscopy using a narrow ($< a$ few arcsec) slit. Based on observations of several sources, nearby ULIRGs are argued to be energetically dominated by highly obscured *compact* (< 1 kpc) nuclear cores, with small contributions from *extended*, modestly obscured starbursts in host galaxies (Soifer et al. 2000; Fischer 2000). The AKARI IRC spectra can directly test whether this argument holds for the majority of nearby ULIRGs.

In this paper, we present the results of systematic 2.5–5 μm slitless spectroscopy of a large number of nearby ULIRGs at $z < 0.3$ using the AKARI IRC. Throughout this paper, $H_0 = 75 \text{ km s}^{-1} \text{ Mpc}^{-1}$, $\Omega_M = 0.3$, and $\Omega_\Lambda = 0.7$ are adopted to be consistent with our previous papers (Imanishi et al. 2006a; Imanishi 2006). The physical scale of $1''$ is 0.74 kpc at $z = 0.040$ (the nearest source), 2.44 kpc at $z = 0.15$, and 3.84 kpc at $z = 0.268$ (the farthest source).

2. Targets

Our targets are basically selected from the list of ULIRGs in the *IRAS* 1 Jy sample (Kim & Sanders 1998). Since AKARI employs the Sun-synchronous polar orbit, flying along the day–night border (Murakami et al. 2007), assigning pointed observations of objects with high ecliptic latitudes is easy due to high visibility, but is difficult for low ecliptic latitude objects. Hence, our sample is biased toward ULIRGs at high ecliptic latitudes, but there is no obvious bias with respect to the physical nature of the sources. ULIRGs at $z > 0.15$ are higher priority than those at $z < 0.15$ because rest-frame 3–4 μm spectroscopy of the $z > 0.15$ sources is possible only with the AKARI IRC. However, ULIRGs at $z < 0.15$ are also included as second priority sources for the following reasons: first, using AKARI IRC slitless spectra, we can measure the total 3.3 μm PAH emission luminosity from entire galactic regions, and then test the previous argument that extended, modestly obscured starbursts in host galaxies are indeed energetically insignificant in ULIRGs (see §1). Second, the AKARI IRC has higher sensitivity at $> 2.5 \mu\text{m}$ and wider wavelength coverage than ground-based *L*-band spectra. Thus, even for ULIRGs at $z < 0.15$, with available ground-based *L*-band spectra, we can better determine the continuum level for the broad 3.1 μm absorption features in higher-quality AKARI IRC spectra. Additionally, absorption features at $\lambda_{\text{rest}} > 4 \mu\text{m}$ (rest-frame), such as CO (4.67 μm) and CO₂ (4.26 μm), can be newly investigated, unless they are redshifted to $\lambda_{\text{obs}} > 5 \mu\text{m}$ (observed frame).

Since our primary scientific aim was to find optically elusive buried AGNs (§1), ULIRGs classified optically as non-Seyferts (i.e., LINER, HII-region, and unclassified) were our main targets. Based on the optical classification by Veilleux et al. (1999), 15 LINER, 12 HII-region, and 6 unclassified ULIRGs at $z > 0.15$ exist in the *IRAS* 1 Jy sample. Among these, 11 LINER, 10 HII-region, and 5 unclassified ULIRGs were observed. In total, AKARI IRC spectra of 26 (of 33) non-Seyfert ULIRGs at $z > 0.15$ in the *IRAS* 1 Jy sample were taken. At $z < 0.15$, 28

LINER, 20 HII-region, and 4 unclassified ULIRGs are listed, of which 8 LINER, 5 HII-region, and 0 unclassified ULIRGs were observed. For ULIRGs optically classified as Seyfert 2s, the presence of energetically significant AGNs surrounded by torus-shaped dust is almost certain, and so these Seyfert 2 ULIRGs were set as a low priority in our project. However, due to good target visibility, four Seyfert 2 ULIRGs were observed. No ULIRGs classified optically as Seyfert 1s (i.e., unobscured broad-line AGN) were observed.

In addition to these ULIRGs in the IRAS 1 Jy sample, the two well-known ULIRGs, UGC 5101 and IRAS 19245–7245 (Super-Antennae), are also included in the sample. The optical classification of UGC 5101 and IRAS 19254–7245 is LINER (Veilleux et al. 1995) and Seyfert 2 (Mirabel et al. 1991), respectively. Both of these sources show clear $3.4 \mu\text{m}$ absorption features in ground-based *L*-band spectra (Imanishi et al. 2001; Imanishi & Maloney 2003; Risaliti et al. 2003). Thus, further investigations of absorption features using high-quality AKARI IRC spectra with wider wavelength coverage are warranted.

In total, 43 ULIRGs in the IRAS 1 Jy sample (39 non-Seyferts and 4 Seyferts) and 2 additional ULIRGs of interest were observed. Table 1 summarizes the basic information and *IRAS*-based infrared properties of the observed ULIRGs.

3. Observations and Data Analysis

Spectroscopic observations were made using the IRC infrared spectrograph (Onaka et al. 2007) onboard the AKARI infrared satellite (Murakami et al. 2007) between October 2006 and August 2007. All data were taken in the mission program named “AGNUL”. Table 2 summarizes the observation log. We used the NG grism mode, which can cover $2.5\text{--}5.0 \mu\text{m}$ simultaneously with an effective spectral resolution of $R \sim 120$ at $3.6 \mu\text{m}$ for point sources (Onaka et al. 2007). The $1 \times 1 \text{ arcmin}^2$ NIR slit was used to minimize the contamination of the spectra by source overlap (Onaka et al. 2007; Ohyama et al. 2007). The pixel scale of AKARI IRC is $1''.46 \times 1''.46$. Only one pointing was assigned for each ULIRG, but since we employed the observing mode of IRC04, one pointing consisted of 8 or 9 independent frames (Onaka et al. 2007) that could be used to remove the effects of cosmic ray hits and obtain spectra of the objects. The total net on-source exposure time was ~ 6 min for each ULIRG.

The spectral analysis was performed in a standard manner using the IDL package prepared for the reduction of AKARI IRC spectra¹. Detailed descriptions are contained in Ohyama et al. (2007). Each frame was dark-subtracted, linearity-corrected, and flat-field corrected. In AKARI IRC slitless spectra, emission more extended than 3–5 pixels ($= 3\text{--}5 \times 1''.46$) was not clearly recognizable, confirming that very extended starburst emission is insignificant. We thus integrated signals within 3–5 pixels for spectral extraction, depending on the actual signal pro-

¹ The actual software package used for our data reduction is “IRC Spectroscopy Toolkit Version 20070913”, which can be found at <http://www.ir.isas.jaxa.jp/ASTRO-F/Observation/DataReduction/IRC/>

file of each ULIRG. The background signal level is estimated from the data points at the both sides of the object position and is subtracted. Wavelength and flux calibrations were made within this package. The wavelength calibration accuracy is taken to be ~ 1 pixel or $\sim 0.01 \mu\text{m}$ (Ohyama et al. 2007). The absolute flux calibration accuracy is $\sim 10\%$ at the central wavelength of the spectra, and can be as large as $\sim 20\%$ at the edge of the NG spectra (close to $2.5 \mu\text{m}$ and $5.0 \mu\text{m}$) (Ohyama et al. 2007). To reduce the scatter of data points, appropriate binning of spectral elements was performed, particularly for faint ULIRGs. The resulting spectral resolution can be as low as $R \sim 50$ at some wavelength range for such faint ULIRGs.

4. Results

Figure 2 presents final infrared $2.5\text{--}5.0 \mu\text{m}$ spectra of ULIRGs obtained with the AKARI IRC. For IRAS 17028+5817, the western (W) and eastern (E) nuclei were resolved with the AKARI IRC, and spectra of both nuclei were of sufficient quality. Spectra of the W (LINER) and E (HII-region) nuclei are thus presented separately, totaling 46 spectra in Figure 2.

Figure 3 compares the spectrum of IRAS 08572+3915 taken with the AKARI IRC and the ground-based IRTF 3m telescope (Imanishi et al. 2006a). Since the infrared dust emission of this ULIRG is dominated by a compact ($< 300\text{pc}$) nuclear core (Soifer et al. 2000), with a very small contribution from extended ($> \text{several kpc}$) starburst activity in the host galaxy, this is an appropriate source to compare AKARI IRC slitless spectrum with the ground-based narrow-slit ($1''6$ -wide) spectrum (Imanishi et al. 2006a). Overall, the spectra agree very well in the overlapped region ($\lambda_{\text{obs}} = 2.9\text{--}4.1 \mu\text{m}$), demonstrating the good calibration accuracy of AKARI IRC spectroscopy. However, when we compare the spectra in more detail, slight discrepancies become apparent at shorter wavelengths; in particular, the flux of the ground-based slit spectrum is smaller than the AKARI IRC slitless spectrum. This discrepancy is larger than the statistical errors of both spectra. In IRAS 08572+3915, although infrared dust emission is dominated by the compact nuclear energy source, *stellar* emission in the extended host galaxy, which becomes more important at shorter wavelengths, may be non-negligible. The slight discrepancy at shorter wavelengths could thus be explained by the scenario that extended stellar emission is covered only by the AKARI IRC slitless spectrum, but not by the ground-based slit spectrum, because of aperture losses.

In Figure 2, although the spectral shapes are rich in variety, most of the observed ULIRGs show emission features at $\lambda_{\text{obs}} \sim (1 + z) \times 3.29 \mu\text{m}$. We ascribe these features to $3.3 \mu\text{m}$ PAH emission because contribution from the Pfd ($\lambda_{\text{rest}} \sim 3.3 \mu\text{m}$; $\sim 10\%$ strength of Br α ; Wynn-Williams 1984) is usually negligible in ULIRGs not classified optically as Seyfert 1s (i.e., unobscured broad-line AGNs) (Imanishi et al. 2006a). To estimate the $3.3 \mu\text{m}$ PAH emission strength, we make the reasonable assumption that the profiles of the $3.3 \mu\text{m}$ PAH emission in these ULIRGs are similar to those of Galactic star-forming regions and nearby starburst galaxies (type-1 sources in Tokunaga et al. 1991), following Imanishi et al. (2006a).

The adopted profile reproduces the observed 3.3 μm PAH emission features of the ULIRGs reasonably well given the adopted continuum levels (shown as solid lines in Figure 2 for PAH-detected ULIRGs) and spectral resolution of the AKARI IRC. Table 3 summarizes the fluxes, luminosities, and rest-frame equivalent widths ($\text{EW}_{3.3\text{PAH}}$) of the 3.3 μm PAH emission feature. The uncertainties of the 3.3 μm PAH fluxes coming from fitting errors and continuum choice are unlikely to exceed $\sim 30\%$ as long as we adopt reasonable continuum levels.

In addition to the 3.3 μm PAH emission features, broad absorption features from ice-covered dust, centered at $\lambda_{\text{rest}} = 3.05\text{--}3.1 \mu\text{m}$ and extending from $\lambda_{\text{rest}} \sim 2.75 \mu\text{m}$ to $\sim 3.55 \mu\text{m}$, are clearly detected in many ULIRGs. Since spectra as short as $\lambda_{\text{obs}} = 2.5 \mu\text{m}$ are covered (as compared to $\lambda_{\text{obs}} = 2.8 \mu\text{m}$ in ground-based L -band spectra; Imanishi et al. 2006a), the continuum level at the shorter wavelength side of the 3.1 μm ice absorption feature is well determined. To estimate the optical depths of the 3.1 μm absorption features ($\tau_{3.1}$), we adopt linear continua (shown as dashed lines in Figure 2 for 3.1 μm -absorption-detected ULIRGs) following Imanishi et al. (2006a). We consider the 3.1 μm absorption feature to be clearly detected only in ULIRGs that display both a significant flux depression below the adopted continuum level at $\lambda_{\text{rest}} = 3.05\text{--}3.1 \mu\text{m}$, and a spectral gap at the 3.3 μm PAH emission feature in which the flux at the shorter wavelength side of this 3.3 μm PAH feature is smaller than that at the longer wavelength side (Imanishi et al. 2006a). The derived $\tau_{3.1}$ values are summarized in column 2 of Table 4. Due to the spectrally broad nature of the 3.1 μm ice absorption feature, the continuum determination has some ambiguity. However, we estimate the typical uncertainty of $\tau_{3.1}$, originating in continuum determination ambiguity and spectral element noise close to the absorption peak, as ~ 0.1 . Since this 3.1 μm ice absorption feature is spectrally intrinsically broad, not consisting of spectrally unresolved narrow lines (Smith et al. 1989), the measured $\tau_{3.1}$ values in AKARI IRC's low-resolution spectra are taken as true ones. For ULIRGs observed with both the AKARI IRC and ground-based telescopes, the presence of the 3.1 μm ice absorption features is generally clearer in AKARI IRC spectra than in ground-based L -band spectra because of the AKARI IRC's higher spectral quality and wider wavelength coverage (e.g., the LINER ULIRG IRAS 09539+0857; Figure 2 of this paper and Imanishi et al. 2006a). IRAS 10091+4704 (LINER), 21477+0502 (LINER), and 04313–1649 (unclassified) may display the 3.1 μm absorption feature, but we do not classify these sources as 3.1 μm -absorption-detected ULIRGs because the continuum ambiguity is large.

In addition to the 3.1 μm ice absorption, absorption features at $\lambda_{\text{rest}} = 3.4 \mu\text{m}$ by bare carbonaceous dust (Pendleton et al. 1994) are found in four ULIRGs: IRAS 08572+3915, 17044+6720, UGC 5101, and IRAS 19254–7245. To estimate the optical depths of the 3.4 μm absorption features ($\tau_{3.4}$) for these sources, we adopt linear continua, which are shown as dashed lines in Figure 2. The estimated $\tau_{3.4}$ values for the four ULIRGs are summarized in column 3 of Table 4.

$\text{Br}\alpha$ ($\lambda_{\text{rest}} = 4.05 \mu\text{m}$) emission is detected in many ULIRGs. However, the $\text{Br}\alpha$ emission

in most cases is spectrally unresolved at AKARI IRC’s resolution ($R \sim 120$), resulting in large uncertainty for the derived flux and luminosity. Br α emission will not be used for our detailed quantitative discussions.

For ULIRGs at $z < 0.1$, AKARI IRC spectral coverage extends to the redshifted CO absorption features centered at $\lambda_{\text{rest}} \sim 4.67 \mu\text{m}$, extending between $\lambda_{\text{rest}} = 4.4\text{--}5.0 \mu\text{m}$ (Spoon et al. 2004; Sani et al. 2008). These features are detected in a few ULIRG spectra (e.g., IRAS 08572+3915, UGC 5101, IRAS 19254–7245). This CO absorption feature consists of many narrow features (Geballe et al. 2006) that are spectrally unresolved with the AKARI IRC ($R \sim 120$). Hence, the apparent optical depths are only lower limits. In IRAS 08572+3915, CO $_2$ absorption features at $\lambda_{\text{rest}} \sim 4.26 \mu\text{m}$ are also discernible. Detailed discussions of these CO and CO $_2$ absorption features will be made by Shirahata et al. (2008).

5. Discussion

We investigate energy sources of observed ULIRGs based on the 3.3 μm PAH emission and 3.1 μm and 3.4 μm absorption features.

5.1. Modestly obscured starbursts

In most of the observed ULIRGs, the presence of starbursts is evident from detection of the 3.3 μm PAH emission. Since dust extinction at 3.3 μm is only $\sim 1/15$ of that in the optical V -band ($\lambda = 0.6 \mu\text{m}$; Rieke & Lebofsky 1985; Lutz et al. 1996), the flux attenuation of 3.3 μm PAH emission with dust extinction of $A_V < 15$ mag is less than 1 mag. Thus, the observed 3.3 μm PAH emission luminosities can be used to quantitatively derive the intrinsic luminosities of modestly obscured ($A_V < 15$ mag) starburst activity. The observed 3.3 μm PAH to infrared luminosity ratios ($L_{3.3\text{PAH}}/L_{\text{IR}}$) are summarized in column 4 of Table 3.

Figures 4a and 4b respectively compare the observed 3.3 μm PAH luminosity ($L_{3.3\text{PAH}}$) and its rest-frame equivalent width ($\text{EW}_{3.3\text{PAH}}$) measured in ground-based slit spectra (abscissa) and in AKARI IRC slitless spectra (ordinate). The abscissa and ordinate of Figure 4a trace nuclear ($< \text{kpc}$) and total starburst luminosities, respectively. If *extended* (several kpc) starbursts in the host galaxies of ULIRGs are energetically much more important than modestly obscured *nuclear* starbursts, then both the $L_{3.3\text{PAH}}$ and $\text{EW}_{3.3\text{PAH}}$ values in the ordinate are expected to be substantially larger than the abscissa. However, the difference in both $L_{3.3\text{PAH}}$ and $\text{EW}_{3.3\text{PAH}}$ is relatively small, a factor of a few at most. We see no evidence that the spatially *extended*, modestly obscured starbursts in host galaxies are substantially (more than an order of magnitude) more luminous than the modestly obscured *nuclear* starbursts in ULIRGs. Even including extended starbursts in host galaxies, the $L_{3.3\text{PAH}}/L_{\text{IR}}$ ratios in ULIRGs are factors of 2.5 to more than 10 times smaller than those found in less infrared-luminous starbursts ($\sim 10^{-3}$; Mouri et al. 1990; Imanishi 2002). Taken at face value, the detected modestly obscured starbursts can account for only $< 10\%$ to at most 40% of the infrared luminosities of the observed

ULIRGs. Our AKARI IRC spectra reinforce the previous arguments, based on a small sample (Soifer et al. 2000), that nearby ULIRGs at $z < 0.3$ are not energetically dominated by extended modestly obscured starburst activity in host galaxies.

5.2. Buried AGNs with weak starbursts

The deficit in observed $3.3 \mu\text{m}$ PAH luminosity relative to the infrared luminosity requires energy sources in addition to the modestly obscured ($A_V < 15$ mag) PAH-emitting starbursts. The first possibility is very highly obscured ($A_V \gg 15$ mag) PAH-emitting starbursts, in which the $3.3 \mu\text{m}$ PAH flux is severely attenuated, while the flux of longer wavelength infrared emission ($8\text{--}1000 \mu\text{m}$) may not be highly attenuated. The second possibility is that an AGN exists that can produce large infrared dust emission luminosities with no PAH emission (see §1), decreasing the observed $L_{3.3\text{PAH}}/L_{\text{IR}}$ ratios. These two scenarios are difficult to differentiate based on the absolute PAH luminosities but can be distinguished by the *equivalent width* of emission or absorption features.

In a normal starburst galaxy, where HII regions, molecular gas, and photodissociation regions are spatially well mixed (Figure 1a), the equivalent width of the $3.3 \mu\text{m}$ PAH-emission feature is insensitive to dust extinction (Imanishi et al. 2006a). If PAH-free AGN emission contributes significantly to the observed $2.5\text{--}5 \mu\text{m}$ flux, then the $\text{EW}_{3.3\text{PAH}}$ value should decrease. The $\text{EW}_{3.3\text{PAH}}$ values in starbursts have an average value of $\text{EW}_{3.3\text{PAH}} \sim 100$ nm, with some scatter, but never become lower than 40 nm (Moorwood 1986). Thus, we adopt $\text{EW}_{3.3\text{PAH}} \lesssim 40$ nm as a strong signature of significant AGN contribution to an observed flux.

Among ULIRGs classified optically as non-Seyferts in the IRAS 1 Jy sample, three LINER ULIRGs, IRAS 23129+2548, 08572+3915, and 17044+6720, and one HII-region ULIRG, IRAS 22088–1831, have $\text{EW}_{3.3\text{PAH}} < 20$ nm (Table 3, column 5), more than a factor of 5 less than typical starburst galaxies. These ULIRGs are strong buried AGN candidates. The following non-Seyfert ULIRGs are also taken to contain luminous buried AGNs because the $\text{EW}_{3.3\text{PAH}}$ values are < 40 nm: the three LINER ULIRGs (IRAS 04074–2801, 11180+1623, and 21477+0502), two HII-region ULIRGs (IRAS 14202+2615 and 17028+5817E), and one optically unclassified ULIRG (IRAS 08591+5248).

5.3. Buried AGNs with coexisting strong starbursts

Based on the $\text{EW}_{3.3\text{PAH}}$ values, we can easily detect buried AGNs with very weak starbursts. Even if strong starburst activity is present, *weakly obscured* AGNs are detectable because weakly attenuated PAH-free continua from the AGNs can dilute the $3.3 \mu\text{m}$ PAH emission considerably. However, detecting *deeply buried* AGNs with coexisting surrounding strong starbursts is very difficult (Figure 1c). Even if the intrinsic luminosities of a buried AGN and surrounding less-obscured starbursts are similar, the AGN flux will be more highly attenuated by dust extinction than the starburst emission. When a buried AGN is obscured by *ice-covered* dust grains, the AGN flux at $\lambda_{\text{rest}} = 3.3 \mu\text{m}$ is attenuated even more severely by

the strong, broad $3.1 \mu\text{m}$ absorption feature, making the $\text{EW}_{3.3\text{PAH}}$ values in observed spectra apparently large.

To determine whether a deeply buried AGN is present in addition to strong starbursts, we use the optical depths of dust absorption features found in the $2.5\text{--}5 \mu\text{m}$ spectra. As described in §1 and in Imanishi et al. (2006a) in more detail, these values can be used to distinguish whether the energy sources are spatially well mixed with dust (a normal starburst), or are more centrally concentrated than the dust (a buried AGN). For a normal starburst with the mixed dust/source geometry in a ULIRG’s core, $\tau_{3.1}$ cannot exceed 0.3, while a buried AGN can produce $\tau_{3.1} > 0.3$ (Imanishi & Maloney 2003; Imanishi et al. 2006a). Therefore, detection of $\tau_{3.1} > 0.3$ can be used to argue for the presence of a buried AGN with a centrally concentrated energy source geometry. Considering the uncertainty of $\tau_{3.1}$ with ~ 0.1 (§4), we classify ULIRGs with $\tau_{3.1} > 0.4$ as buried AGN candidates.

Aside from the above ULIRGs with low $\text{EW}_{3.3\text{PAH}}$, the following non-Seyfert ULIRGs in the IRAS 1 Jy sample are newly classified as buried AGNs: ten LINER ULIRGs (IRAS 05020–2941, 09463+8141, 11028+3130, 14121–0126, 16333+4630, 00482–2721, 09539+0857, 10494+4424, 16468+5200, 17028+5817W), four HII-region ULIRGs (IRAS 01199–2307, 01355–1814, 17068+4027, 11387+4116), and one optically unclassified ULIRG (IRAS 01494–1845). This large $\tau_{3.1}$ method is sensitive to deeply buried AGNs but obviously misses weakly obscured AGNs, which are more easily detected with the above low $\text{EW}_{3.3\text{PAH}}$ method. Hence, the large $\tau_{3.1}$ and low $\text{EW}_{3.3\text{PAH}}$ methods are used in complementary fashion to detect AGN signatures.

We can also investigate the dust/source geometry from the $\tau_{3.4}$ value. ULIRGs with $\tau_{3.4} > 0.2$ can be used to argue for the presence of buried AGNs (Imanishi & Maloney 2003; Imanishi et al. 2006a). Among the optically non-Seyfert ULIRGs in the IRAS 1 Jy sample, only the LINER ULIRG IRAS 08572+3915 displays $\tau_{3.4} > 0.2$. The LINER ULIRG of interest, UGC 5101, and the Seyfert 2 ULIRG, IRAS 19254–7245, also show $\tau_{3.4} > 0.2$. However, all of these three ULIRGs have already been classified as having luminous AGNs based on their low $\text{EW}_{3.3\text{PAH}}$ values.

Imanishi et al. (2006a, 2007a) commented that exceptionally centrally concentrated starbursts (Figure 1d) and normal starbursts with mixed dust/source geometry obscured by foreground dust in edge-on host galaxies (Figure 1e) can also produce large $\tau_{3.1}$ and $\tau_{3.4}$ values, but argued that it is very unlikely for the bulk of ULIRGs with $\tau_{3.1} > 0.3$ and/or $\tau_{3.4} > 0.2$ to correspond to these non-AGN cases.

For the remaining non-Seyfert ULIRGs with $\text{EW}_{3.3\text{PAH}} > 40 \text{ nm}$, $\tau_{3.1} \lesssim 0.4$, and $\tau_{3.4} \lesssim 0.2$, no obvious buried AGN signatures were observed in the $2.5\text{--}5 \mu\text{m}$ spectra. Their spectra can be explained by either of the following scenarios: normal starbursts with mixed dust/source geometry are energetically dominant, or AGNs are present, but the AGN emission is so highly attenuated that its contribution to the observed $2.5\text{--}5 \mu\text{m}$ flux is not significant. We have no

way of distinguishing between these two scenarios. However, some examples are known (e.g., NGC 4418) in which buried AGN signatures are found only at wavelengths longer than $5 \mu\text{m}$ (Imanishi et al. 2004; Dudley & Wynn-Williams 1997; Spoon et al. 2001). Thus, the detected buried AGN fraction in the $2.5\text{--}5 \mu\text{m}$ AKARI IRC spectra is only a lower limit.

5.4. *Dust extinction and intrinsic AGN luminosities*

In a buried AGN with centrally concentrated energy source geometry, dust at a temperature of 1000 K, which is close to the innermost dust sublimation radius, produces continuum emission with a peak at $\lambda \sim 3 \mu\text{m}$, assuming approximately blackbody emission. Since a foreground screen dust distribution model is applicable to a buried AGN (Imanishi et al. 2006a, 2007a), the $\tau_{3.1}$ (ice-covered dust) and $\tau_{3.4}$ (bare dust) values reflect the dust column density toward the $3 \mu\text{m}$ continuum-emitting region, which is almost equal to the column density toward the buried AGN itself (Imanishi et al. 2006a, 2007a).

The $3.1 \mu\text{m}$ absorption feature is detectable if ice-covered dust grains are present in front of the $3\text{--}4 \mu\text{m}$ continuum emitting energy source. Such ice-covered dust grains are usually found deep inside molecular gas, where ambient UV radiation is sufficiently shielded (Whittet et al. 1988; Tanaka et al. 1990; Smith et al. 1993; Murakawa et al. 2000). The $3.4 \mu\text{m}$ absorption feature should be detected if the $3\text{--}4 \mu\text{m}$ continuum emitting energy source is obscured by bare carbonaceous dust grains (Pendleton et al. 1994; Imanishi et al. 1996; Rawlings et al. 2003), but is undetected if the absorbing dust is ice-covered (Mennella et al. 2001). Since absorbing dust consists of both bare and ice-covered dust grains, ULIRGs with obscured energy sources should show both features, and the true dust column density is derivable from a proper combination of $\tau_{3.1}$ and $\tau_{3.4}$.

However, despite the detection of the $3.1 \mu\text{m}$ ice absorption features in many ULIRGs, only two ULIRGs in the IRAS 1 Jy sample, IRAS 08572+3915 and 17044+6720, show clear $3.4 \mu\text{m}$ carbonaceous dust absorption features. Even including the two sources of interest, UGC 5101 and IRAS 19254–7245, only four ULIRGs display clearly detectable $3.4 \mu\text{m}$ absorption features. The difference in the detection rate largely comes from the intrinsically smaller oscillator strength of the $3.4 \mu\text{m}$ carbonaceous dust absorption feature ($\tau_{3.4}/A_V = 0.004\text{--}0.007$; Pendleton et al. 1994) compared to the $3.1 \mu\text{m}$ ice absorption feature ($\tau_{3.1}/A_V = 0.06$; Tanaka et al. 1990; Smith et al. 1993; Murakawa et al. 2000). Even if a modestly large amount of bare carbonaceous dust grains is present in front of the continuum-emitting energy source, the $\tau_{3.4}$ value is small, making the detection of the $3.4 \mu\text{m}$ dust absorption feature difficult. Additionally, the $3.3 \mu\text{m}$ PAH emission feature is often accompanied by a sub-peak at $3.4 \mu\text{m}$ (Tokunaga et al. 1991; Imanishi & Dudley 2000), and this sub-peak may dilute the $3.4 \mu\text{m}$ dust absorption feature at the same wavelength. In fact, all the four ULIRGs with detectable $3.4 \mu\text{m}$ absorption features are limited to relatively weak PAH emitters ($\text{EW}_{3.3\text{PAH}} < 35 \text{ nm}$). Finally, when the spectrally broad $3.1 \mu\text{m}$ absorption feature is strong, the absorption feature

extends to the longer wavelength side of the $3.3 \mu\text{m}$ PAH emission feature, making it difficult to distinguish the origin of the apparent flux depression at $\lambda_{\text{rest}} \sim 3.4 \mu\text{m}$. Among the four sources with detectable $3.4 \mu\text{m}$ absorption features, IRAS 08572+3915, 17044+6720, and 19254–7245 indeed display only weak or undetectable $3.1 \mu\text{m}$ absorption features. The remaining source, UGC 5101, shows large $\tau_{3.1}$, but we can recognize the $3.4 \mu\text{m}$ absorption feature, primarily because UGC 5101 is one of the brightest sources and the signal to noise ratios are among the highest. Detection of the $3.4 \mu\text{m}$ absorption features in the remaining ULIRGs with large $\text{EW}_{3.3\text{PAH}}$, large $\tau_{3.1}$, and limited signal-to-noise ratios in the continuum is basically difficult. Therefore, while the total dust column density can be estimated in a reasonably reliable way for ULIRGs with both detectable $3.1 \mu\text{m}$ and $3.4 \mu\text{m}$ absorption features, the estimated dust column densities are only lower limits, and should be much smaller than the actual values for ULIRGs with only detectable $3.1 \mu\text{m}$ absorption features. The estimated dust column densities are summarized in column 4 of Table 4.

In a buried AGN, the surrounding dust has a strong temperature gradient in that inner dust, close to the central energy source, has higher temperature than outer dust. Luminosity is transferred at each temperature, and the intrinsic luminosity of inner hot dust emission at $3\text{--}4 \mu\text{m}$ (νF_ν) should be comparable to that of outer cool dust emission at $60 \mu\text{m}$, the wavelength which dominates the observed infrared emission of ULIRGs (Sanders et al. 1988a). Thus, if the intrinsic AGN’s $3\text{--}4 \mu\text{m}$ luminosity (νF_ν) is comparable to the observed infrared luminosities of ULIRGs, then we can argue that the buried AGN is energetically important. For ULIRGs with low $\text{EW}_{3.3\text{PAH}}$ ($<40 \text{ nm}$), we can roughly extract the AGN’s PAH-free continuum at $3\text{--}4 \mu\text{m}$, based on the assumption that starburst activity intrinsically shows $\text{EW}_{3.3\text{PAH}} \sim 100 \text{ nm}$. That is, for ULIRGs with $\text{EW}_{3.3\text{PAH}} = 30 \text{ nm}$ (30% of the typical starburst value), we consider that 70% of the $3\text{--}4 \mu\text{m}$ continuum comes from AGN’s PAH-free continuum emission. Thus, we can estimate the *observed* $3\text{--}4 \mu\text{m}$ flux of AGN emission. Next, for ULIRGs with both detectable $3.1 \mu\text{m}$ and $3.4 \mu\text{m}$ absorption features (IRAS 08572+3915, UGC 5101, and IRAS 19254–7245), and for IRAS 17044+6720, which displays only the $3.4 \mu\text{m}$ absorption feature, we can estimate dust column density, or *dust extinction*, toward the $3\text{--}4 \mu\text{m}$ continuum emitting regions based on $\tau_{3.1}$ and $\tau_{3.4}$. When we combine the *observed* AGN flux at $3\text{--}4 \mu\text{m}$ and *dust extinction* toward the $3\text{--}4 \mu\text{m}$ continuum emitting regions, we can derive the dust-extinction-corrected *intrinsic* AGN flux, and thus the intrinsic AGN luminosity. If we adopt $A_{3\text{--}4\mu\text{m}}/A_V \sim 0.058$ (Rieke & Lebofsky 1985), then we find $\tau_{3.1}/A_{3\text{--}4\mu\text{m}} \sim 1$ and $\tau_{3.4}/A_{3\text{--}4\mu\text{m}} \sim 0.069\text{--}0.12$ for the Galactic interstellar medium. Assuming this relationship, we estimate the intrinsic AGN luminosities at $3\text{--}4 \mu\text{m}$ (νF_ν) to be $L \gtrsim 10^{12} L_\odot$ in all the $3.4\mu\text{m}$ -absorption-detected ULIRGs. The putative AGN activity is therefore energetically sufficient to quantitatively account for the bulk of the infrared luminosities of these ULIRGs ($L_{\text{IR}} \sim 10^{12} L_\odot$).

5.5. Dependence of the buried AGN fraction on optical spectral type: LINER vs. HII-region

In total, AKARI IRC 2.5–5 μm spectra of 19 LINER, 16 HII-region, and 5 optically unclassified ULIRG’s nuclei in the *IRAS* 1 Jy sample were obtained. The low $\text{EW}_{3.3\text{PAH}}$ method suggests six LINER and three HII-region ULIRG’s nuclei contain luminous buried AGNs (§5.2). In addition to these ULIRGs, the large $\tau_{3.1}$ method classifies ten LINER and four HII-regions ULIRG’s nuclei as sources with deeply obscured buried AGNs (§5.3). In total, the detected buried AGN fraction is 16/19 (84%) for LINER ULIRGs, and 7/16 (44%) for HII-region ULIRGs (Table 4, columns 5 and 6). Since the selection of the observed ULIRGs is based solely on the target’s visibility from the AKARI satellite and should be unbiased in terms of their energy sources (§2), we argue that the detected buried AGN fraction is higher in LINER ULIRGs than in HII-region ULIRGs. The same result was found from ground-based *L*-band spectroscopy and Spitzer 5–35 μm spectroscopy of ULIRGs at $z < 0.15$ (Imanishi et al. 2006a, 2007a), and also from a VLA radio observational search for compact radio core emission (another good AGN indicator) (Nagar et al. 2003). Therefore, we confirm that a larger fraction of LINER ULIRGs possess luminous buried AGNs than HII-region ULIRGs with a probability of $\sim 99\%$.

The higher buried AGN fraction in optically LINER ULIRGs can be explained qualitatively by a dustier starburst scenario (Imanishi et al. 2007a). For starburst/buried AGN composite ULIRGs (Figure 1c), the optical LINER or HII-region classifications are likely largely affected by the properties of the modestly obscured starbursts at the exteriors of the buried AGN, rather than by buried AGN-related emission, as optical observations can probe only the surfaces of dusty objects. In a dusty starburst, shock-related emission can be relatively important in the optical compared to the emission from the HII-regions themselves, resulting in optical LINER classification.

When a luminous AGN is placed at the center of a *less dusty* starburst classified optically as an HII-region, the AGN emission is more easily detectable in the optical, making such an object an optical Seyfert. In contrast, when a luminous AGN is placed at the center of a *dusty* starburst classified optically as a LINER, the AGN emission is more elusive in the optical, so that such an object is classified as an optical non-Seyfert. Hence, this scenario can explain the observed higher fraction of optically elusive *buried* AGNs in optically LINER ULIRGs compared to HII-region ULIRGs. In fact, the emission probed in the optical was found to be dustier in LINER ULIRGs than in HII-region ULIRGs (Veilleux et al. 1995, 1999).

5.6. The buried AGN fraction as a function of infrared luminosity

Due to the inclusion of ULIRGs at $z > 0.15$, we have now a large number of ULIRGs with $L_{\text{IR}} \gtrsim 10^{12.3}L_{\odot}$. Specifically, only 1 of 13 observed non-Seyfert ULIRGs at $z < 0.15$ has $L_{\text{IR}} \gtrsim 10^{12.3}L_{\odot}$, while 16 of 26 observed non-Seyfert ULIRGs at $z > 0.15$ have $L_{\text{IR}} \gtrsim 10^{12.3}L_{\odot}$ (see Table 1). We can thus investigate the buried AGN fraction, separating ULIRGs into two categories: those with $L_{\text{IR}} < 10^{12.3}L_{\odot}$ and those with $L_{\text{IR}} \gtrsim 10^{12.3}L_{\odot}$.

Among the observed non-Seyfert ULIRGs in the IRAS 1 Jy sample, 22 sources have $L_{\text{IR}} < 10^{12.3}L_{\odot}$ and the remaining 17 sources have $L_{\text{IR}} \gtrsim 10^{12.3}L_{\odot}$. Based on the buried AGN signatures in Table 4, the fraction of ULIRGs with detectable buried AGN signatures is 12/22 (= 55%) for non-Seyfert ULIRGs with $L_{\text{IR}} < 10^{12.3}L_{\odot}$ and 12/17 (= 71%) for non-Seyfert ULIRGs with $L_{\text{IR}} \gtrsim 10^{12.3}L_{\odot}$. Although the total sample size is not large, we find a higher buried AGN fraction with increasing ULIRG infrared luminosity. Imanishi et al. (2006a) investigated, based on ground-based L -band (2.8–4.1 μm) spectra, the buried AGN fraction in a larger number of ULIRGs at $z < 0.15$ in the IRAS 1 Jy sample than in this paper. Several ULIRGs at $z < 0.15$ studied in this paper are also included in this ground-based study. When we divide the observed ULIRGs by Imanishi et al. (2006a) into those with $L_{\text{IR}} < 10^{12.3}L_{\odot}$ and $\gtrsim 10^{12.3}L_{\odot}$, the detected buried AGN fraction is 16/29 (= 55%) in non-Seyfert ULIRGs with $L_{\text{IR}} < 10^{12.3}L_{\odot}$, and 6/9 (= 67%) in non-Seyfert ULIRGs with $L_{\text{IR}} \gtrsim 10^{12.3}L_{\odot}$. The detected buried AGN fractions in ground-based and AKARI IRC spectra are comparable for non-Seyfert ULIRGs with both $L_{\text{IR}} < 10^{12.3}L_{\odot}$ ($\sim 55\%$) and $\gtrsim 10^{12.3}L_{\odot}$ ($\sim 70\%$). We therefore argue that the detected buried AGN fraction increases with ULIRG infrared luminosity. This trend parallels the higher detection rate of optical Seyfert signatures in ULIRGs with higher infrared luminosities (Veilleux et al. 1999).

The fraction of both optical Seyferts and luminous buried AGNs is significantly smaller in galaxies with $L_{\text{IR}} < 10^{12}L_{\odot}$ than ULIRGs (Veilleux et al. 1999; Soifer et al. 2001). Hence, we conclude that AGN activity becomes more important as the infrared luminosities of galaxies increase. Recently, the so-called galaxy downsizing phenomena have been found, where galaxies with currently larger stellar masses have finished their major star-formation in earlier cosmic age (Cowie et al. 1996; Bundy et al. 2005). AGN feedbacks are proposed to be responsible for the galaxy downsizing phenomena (Granato et al. 2004; Bower et al. 2006; Croton et al. 2006). Namely, in galaxies with currently larger stellar masses, AGN feedbacks have been stronger in the past, and gas has been expelled in a shorter time scale. Buried AGNs can have particularly strong feedbacks, because the AGNs are surrounded by a large amount of nuclear gas and dust. If we reasonably assume that galaxies with currently larger stellar masses have previously been more infrared luminous, then the detected higher buried AGN fraction in more infrared luminous galaxies may support the AGN feedback scenario as the origin of the galaxy downsizing phenomena ².

² To form more stars, more star-formation should have been occurred in the past, producing stronger star-formation related infrared emission in the past. If AGN's energetic contribution is negligible in LIRGs with $L_{\text{IR}} < 10^{12}L_{\odot}$, but important, say $\sim 50\%$, in ULIRGs with $L_{\text{IR}} > 10^{12}L_{\odot}$, then AGN feedbacks can be stronger in ULIRGs, and yet higher infrared luminosity ($\sim 5 \times 10^{11}L_{\odot}$) can come from star-forming activity in ULIRGs, producing more stellar masses in ULIRGs than in LIRGs.

5.7. Comparison with Seyfert 2 ULIRGs

We compare the 2.5–5 μm spectral properties of non-Seyfert ULIRGs showing buried AGN signatures with those of Seyfert 2 ULIRGs (i.e., known obscured-AGN-possessing ULIRGs). The apparent main difference between them is that the ionizing radiation from the putative buried AGNs in non-Seyfert ULIRGs is obscured by the surrounding dust along virtually all lines-of-sight; in contrast, dust around the AGNs in Seyfert 2 ULIRGs is distributed in a “torus”, and ionizing radiation from the AGNs can escape along the torus axis, allowing for optical Seyfert signature detection (Figure 5).

The four ULIRGs classified optically as Seyfert 2s in the IRAS 1 Jy sample show no clear absorption features at 2.5–5 μm . Imanishi et al. (2006a) also found in ground-based L -band spectra that the fraction of optically classified Seyfert 2 ULIRGs showing strong dust absorption features is substantially smaller than buried AGNs in optically non-Seyfert ULIRGs. We thus argue that the line-of-sight dust column density toward the AGNs is lower in Seyfert 2 ULIRGs than buried AGNs in non-Seyfert ULIRGs. Thus, buried AGNs and Seyfert 2 AGNs (obscured by torus-shaped dust) differ not only in dust geometry, but also in dust column density along our line-of-sight; specifically, the dust columns toward the buried AGNs are much higher (Imanishi et al. 2006a). Since the dust covering factor around buried AGNs (almost all directions) is also larger than Seyfert 2 AGNs (torus-shaped), the total amount of nuclear dust must be larger in the former (Figure 5).

Since the gas and dust in an AGN have angular momentum with respect to the central supermassive black hole, an axisymmetric spatial distribution is more natural than a spherical geometry. In this case, the column densities can be high in certain directions but low in others (Figure 5). For a fixed angular momentum, the dust column density ratios between the highest and lowest column directions are similar among different galaxies. If the total amount of nuclear dust is modest, the direction of the lowest dust column density can be transparent to the AGN’s ionizing radiation, making Seyfert signatures detectable in the optical spectra. As the total amount of nuclear dust increases, even the direction of the lowest dust column density can be opaque to the AGN’s ionizing radiation, making such galaxies optically elusive buried AGNs. Thus, all of the observed spectral properties of buried AGNs and Seyfert-type AGNs are explicable given a larger amount of nuclear dust in the former. Since ULIRGs contain a large amount of nuclear gas and dust (Sanders & Mirabel 1996), the high buried AGN fraction is inevitable. Understanding optically elusive buried AGNs is therefore essential if we are to unveil the true nature of the ULIRG population.

5.8. Dependence on far-infrared colors

Based on the *IRAS* 25 μm to 60 μm flux ratio (f_{25}/f_{60}), ULIRGs are divided into cool (< 0.2) and warm (> 0.2) sources (Sanders et al. 1988b). Many of the non-Seyfert ULIRGs with detectable buried AGN signatures show cool far-infrared colors (Table 1). Although AGNs

classified optically as Seyferts usually show warm far-infrared colors (de Grijp et al. 1987; Keel et al. 2005), cool far-infrared colors of buried AGNs are the natural consequence of a large amount of nuclear dust, where contributions from the outer, cooler dust components to the infrared radiation become more important than for optical Seyferts.

Figure 6(a) compares *IRAS* 25 μm to 60 μm flux ratios (i.e., far-infrared color) with the observed 3.3 μm PAH to infrared luminosity ratios ($L_{3.3\text{PAH}}/L_{\text{IR}}$). Seyfert ULIRGs tend to appear in the warmer far-infrared color range than non-Seyfert ULIRGs, as expected from the decreased amount of nuclear dust in the former (§5.7). No systematic difference in the $L_{3.3\text{PAH}}/L_{\text{IR}}$ ratios between non-Seyfert and Seyfert ULIRGs exists.

Figure 6(b) compares the far-infrared colors and $\text{EW}_{3.3\text{PAH}}$ for non-Seyfert ULIRGs. Buried AGNs appear in both the warm and cool ranges. Although it is sometimes argued that ULIRGs with cool far-infrared colors must be starburst-dominated, simply because Seyfert-type AGNs show warm far-infrared colors (e.g., Downes & Solomon 1998), we do not confirm this to be true for the heavily buried AGNs.

6. Summary

We present the results of infrared 2.5–5 μm AKARI IRC slitless spectroscopy of a large sample of nearby ULIRGs at $z < 0.3$ from the *IRAS* 1 Jy sample. We mainly observed ULIRGs with no obvious optical Seyfert signatures (i.e., LINER, HII-region, and unclassified). One ULIRG showed bright resolvable double nuclei, and spectra of 19 LINER, 16 HII-region, and 5 optically unclassified ULIRG nuclei were obtained in total. In addition to these non-Seyfert ULIRGs, four Seyfert 2 ULIRGs and two well-known ULIRGs were observed. Using the 3.3 μm PAH emission, 3.1 μm ice absorption, and 3.4 μm bare carbonaceous dust absorption features, we investigated whether the infrared 2.5–5 μm spectra of the non-Seyfert ULIRGs could be explained solely by starbursts, or whether the ULIRGs displayed signatures of luminous, but optically elusive, *buried* AGNs. The AKARI IRC’s 2.5–5 μm wavelength coverage, unaffected by Earth’s atmospheric window, enabled us to unambiguously distinguish between absorption-dominated and emission-dominated sources, even for ULIRGs at $z > 0.15$, which was impossible with ground-based *L*-band (2.8–4.1 μm) spectroscopy.

Our main conclusions are the following.

1. The 3.3 μm PAH emission, the starburst probe, was detected in all but four non-Seyfert ULIRGs. The intrinsic luminosities of modestly obscured ($A_V < 15$ mag) starbursts were roughly estimated from the observed 3.3 μm PAH emission luminosities. We found no substantial enhancement of the 3.3 μm PAH luminosities and equivalent widths in the AKARI IRC slitless spectra compared to ground-based slit spectra. The observed 3.3 μm PAH to infrared luminosity ratios were smaller by a factor of 2.5 to >10 compared to those found in less infrared-luminous starbursts, suggesting that detected modestly obscured

starbursts, even including spatially extended (several kpc) ones in the host galaxies probed by AKARI, are energetically insignificant as the origin of the large ULIRG’s infrared dust emission luminosities.

2. Among the optically non-Seyfert ULIRGs in the IRAS 1 Jy sample, six LINER, three HII-region, and one unclassified ULIRG’s nuclei showed $3.3 \mu\text{m}$ PAH emission equivalent widths ($\text{EW}_{3.3\text{PAH}}$), which were much smaller than typical values found in starburst galaxies. A strong contribution from the AGN’s PAH-free continua to the observed $2.5\text{--}5 \mu\text{m}$ fluxes was suggested.
3. Besides these low $\text{EW}_{3.3\text{PAH}}$ ULIRGs, the optical depths of $3.1 \mu\text{m}$ ice ($\tau_{3.1}$) and $3.4 \mu\text{m}$ bare carbonaceous dust ($\tau_{3.4}$) absorption features were used to determine whether the energy sources at the cores of ULIRGs are more centrally concentrated than the surrounding dust (as is expected for a buried AGN), or are spatially well mixed with dust (a normal starburst). The large optical depths in ten LINER, four HII-region, and one unclassified ULIRG’s nuclei suggested that the energy sources are more centrally concentrated than the surrounding dust. These ULIRGs were also classified as displaying signatures of luminous buried AGNs in addition to detectable starburst activity.
4. In total, 16/19 (84%) LINER, 7/16 (44%) HII-region, and 2/5 (40%) optically unclassified ULIRG’s nuclei showed some buried AGN signatures, based either on the low $\text{EW}_{3.3\text{PAH}}$ method or on the large $\tau_{3.1}$ ($\tau_{3.4}$) method. The higher detection rate of buried AGNs in LINER ULIRGs than in HII-region ULIRGs was similar to previous results based on ground-based L -band ($2.8\text{--}4.1 \mu\text{m}$) spectroscopy and Spitzer $5\text{--}35 \mu\text{m}$ spectroscopy of ULIRGs at $z < 0.15$. This trend can be explained qualitatively by a dustier starburst scenario in LINER ULIRGs than in HII-region ULIRGs.
5. We found that the fraction of buried AGNs increases with increasing infrared luminosity. This may support the AGN-feedback scenario as the origin of galaxy downsizing phenomena.
6. We confirmed the following main trends, as previously seen in ground-based L -band spectroscopy of ULIRGs at $z < 0.15$: (1) The fraction of sources with large dust absorption optical depths is higher in buried AGNs in non-Seyfert ULIRGs than ULIRGs classified optically as Seyfert 2s. (2) Luminous buried AGN signatures were detected in ULIRGs with both warm and cool far-infrared colors. These results can reasonably be explained by the scenario that buried AGNs in optically non-Seyfert ULIRGs contain a systematically larger amount of nuclear dust than optical Seyfert 2s (= AGNs obscured by torus-shaped dust), making even the direction of the lowest dust column density opaque to the AGN’s ionizing radiation. The high buried AGN fraction in ULIRGs is inevitable, given their high nuclear dust concentration. Therefore, understanding optically elusive buried AGNs in the dusty ULIRG population is very important.

More non-Seyfert ULIRGs in the IRAS 1 Jy sample, and lower infrared luminosity

galaxies ($L_{\text{IR}} = 10^{11-12}L_{\odot}$), are scheduled to be observed spectroscopically with the AKARI IRC during AKARI phase 3. The above conclusions will be then tested based on a statistically larger sample size than in the present paper.

This work is based on observations with AKARI, a JAXA project with the participation of ESA. We thank the AKARI IRC instrument team, particularly H. Matsuhara and D. Ishihara, for making this study possible. Data presented herein were obtained at the W.M. Keck Observatory from telescope time allocated to the National Aeronautics and Space Administration through the agency's scientific partnership with the California Institute of Technology and the University of California. The Observatory was made possible by the generous financial support of the W.M. Keck Foundation. We thank the anonymous referee for his/her useful comments. M.I. is supported by Grants-in-Aid for Scientific Research (19740109). Part of the data analysis was performed using a computer system operated by the Astronomical Data Analysis Center (ADAC) and the Subaru Telescope of the National Astronomical Observatory, Japan. This research made use of the SIMBAD database, operated at CDS, Strasbourg, France, and of the NASA/IPAC Extragalactic Database (NED) operated by the Jet Propulsion Laboratory, California Institute of Technology, under contract with the National Aeronautics and Space Administration.

7. Appendix A

Imanishi et al. (2006a) presented ground-based L -band ($2.8\text{--}4.1\ \mu\text{m}$) spectra of a large number of non-Seyfert ULIRGs at $z < 0.15$ in the IRAS 1 Jy sample (Kim & Sanders 1998). However, the sample is not statistically complete, and unobserved non-Seyfert ULIRGs remain in this sample. After the publication of Imanishi et al. (2006a), ground-based L -band spectra of six such unobserved non-Seyfert ULIRGs, and two ULIRGs classified optically as Seyfert 2s, (Table 5), were obtained.

Observations of these ULIRGs were made using the IRCS infrared spectrograph (Kobayashi et al. 2000) attached to the Nasmyth focus of the Subaru 8.2-m telescope (Iye et al. 2004), and the NIRSPEC infrared spectrograph (McLean et al. 1998) attached to the Nasmyth focus of the Keck II 10-m telescope. The observing log is summarized in Table 5. For both observing runs, the sky was clear and the seeing at K ($2\text{--}2.5\ \mu\text{m}$), measured in images taken before L -band spectroscopy, was $\sim 0''.4\text{--}0''.9$ full-width at half-maximum (FWHM).

For Subaru IRCS observing runs, a $0''.9$ -wide slit and the L -grism were used with a 52-mas pixel scale. The achievable spectral resolution was $R \sim 140$ at $\lambda \sim 3.5\ \mu\text{m}$. The slit length was $18''$. A standard telescope nodding technique (ABBA pattern), with a throw of $7''$ along the slit, was employed to subtract background emission. Subaru’s optical guider was used to monitor the telescope tracking. Exposure time was $0.8\text{--}1.2$ s, and 50–60 coadds were made at each nod position.

For Keck II NIRSPEC observing runs, low-resolution long-slit spectroscopy was employed with a $0''.76$ -wide (4 pixel) slit and the KL ($2.16\text{--}4.19\ \mu\text{m}$) filter. The achievable spectral resolution was $R \sim 1100$. The slit length was $42''$. A standard telescope nodding technique (ABBA pattern), with a throw of $15''$ along the slit, was employed to subtract background emission. The telescope tracking was monitored based on the infrared K -band image on the SCAM, the slit viewer of NIRSPEC. Exposure time was $0.5\text{--}0.6$ s, and 40–120 coadds were made at each nod position.

Appropriate standard stars (Table 5) were observed, with an air mass difference of < 0.1 compared to individual ULIRGs to correct for the transmission of Earth’s atmosphere. The L -band magnitudes of the standard stars were estimated based on their V -band ($0.6\ \mu\text{m}$) magnitudes and $V\text{--}L$ colors of the corresponding stellar types (Tokunaga 2000).

Standard data analysis procedures were employed using IRAF³. Initially, frames taken with an A (B) beam were subtracted from frames subsequently taken with a B (A) beam, and the resulting subtracted frames were added and divided by a spectroscopic flat image. Then, bad pixels and pixels hit by cosmic rays were replaced with interpolated values of sur-

³ IRAF is distributed by the National Optical Astronomy Observatories, which are operated by the Association of Universities for Research in Astronomy, Inc. (AURA), under cooperative agreement with the National Science Foundation.

rounding pixels. Finally the spectra of ULIRG's nuclei and standard stars were extracted by integrating signals over $1''.1$ – $2''.7$, depending on actual signal profiles. Wavelength calibration was performed, taking into account the wavelength-dependent transmission of Earth's atmosphere. The spectra of ULIRG's nuclei were divided by the observed spectra of standard stars, multiplied by the spectra of blackbodies with temperatures appropriate to individual standard stars (Table 5).

Flux calibration was conducted based on the signals of ULIRGs and standard stars detected inside our slit spectra. To reduce the scatter of data points, appropriate binning of spectral elements was performed, particularly at $\lambda_{\text{obs}} < 3.3 \mu\text{m}$ and $> 3.9 \mu\text{m}$, where the scatter is large due to poor atmospheric transmission and/or large background emission.

Figure 7 presents the final spectra of these eight ULIRGs. Table 6 summarizes the strengths of the $3.3 \mu\text{m}$ PAH emission features. Among the six ULIRGs classified optically as non-Seyferts, the low $\text{EW}_{3.3\text{PAH}}$ value of the HII-region ULIRG, IRAS 01004–2237 ($\sim 30 \text{ nm}$; Table 6), suggests the significant contribution from a buried AGN to the observed 3 – $4 \mu\text{m}$ flux.

References

- Bower, R. G., Benson, A. J., Malbon, R., Helly, J. C., Frenk, C. S., Baugh, C. M., Cole, S., & Lacey, C. G. 2006, *MNRAS*, 370, 645
- Bundy, K., Ellis, R. S., & Conselice, C. J. 2005, *ApJ*, 625, 621
- Cowie, L. L., Songaila, A., Hu, E. M., & Cohen, J. G. 1996, *AJ*, 112, 839
- Croton, D. J., et al. 2006, *MNRAS*, 365, 11
- de Grijp, M. H. K., Miley, G. K., & Lub, J. 1987, *A&AS*, 70, 95
- Downes, D., & Solomon, P. M. 1998, *ApJ*, 507, 615
- Dudley, C. C., & Wynn-Williams, C. G. 1997, *ApJ*, 488, 720
- Fischer, J. 2000, in *ISO Beyond the Peaks*, ed. A. Salama, M. F. Kessler, K. Leech, & B. Schulz (ESA SP-456; Noordwijk: ESA), 239 (astro-ph/0009395)
- Geballe, T. R., Goto, M., Usuda, T., Oka, T., & McCall, B. J. 2006, *ApJ*, 644, 907
- Granato, G. L., De Zotti, G., Silva, L., Bressan, A., & Danese, L. 2004, *ApJ*, 600, 580
- Imanishi, M. 2002, *ApJ*, 569, 44
- Imanishi, M. 2006, *AJ*, 131, 2406
- Imanishi, M., & Dudley, C. C. 2000, *ApJ*, 545, 701
- Imanishi, M., & Maloney, P. R. 2003, *ApJ*, 588, 165
- Imanishi, M., Dudley, C. C., & Maloney, P. R. 2001, *ApJ*, 558, L93
- Imanishi, M., Dudley, C. C., & Maloney, P. R. 2006a, *ApJ*, 637, 114
- Imanishi, M., Dudley, C. C., Maiolino, R., Maloney, P. R., Nakagawa, T., & Risaliti, G. 2007a, *ApJS*, 171, 72
- Imanishi, M., Nakanishi, K., & Kohno, K. 2006b, *AJ*, 131, 2888
- Imanishi, M., Nakanishi, K., Tamura, Y., Oi, N., & Kohno, K. 2007b, *AJ*, 134, 2366
- Imanishi, M., Nakanishi, K., Kuno, N., & Kohno, K. 2004, *AJ*, 128, 2037

Imanishi, M., Sasaki, Y., Goto, M., Kobayashi, N., Nagata, T., & Jones, T. J. 1996, *AJ*, 112, 235
 Iye, M. et al., 2004, *PASJ*, 56, 381
 Keel, W. C., Irby, B. K., May, A., Miley, G. K., Golombek, D., de Grijp, M. H. K., & Gallimore, J. F. 2005, *ApJS*, 158, 139
 Kim, D. -C., & Sanders, D. B., 1998, *ApJS*, 119, 41
 Kobayashi, N., et al. 2000, *Proc. SPIE* 4008, 1056
 Le Floc'h et al. 2005, *ApJ*, 632, 169
 Lutz, D. et al. 1996, *A&A*, 315, L269
 Maiolino, R. et al. 2003, *MNRAS*, 344, L59
 McLean, I. S., et al. 1998, *Proc. SPIE*, 3354, 566
 Mennella, V., Munoz Caro, G. M., Ruiterkamp, R., Schutte, W. A., Greenberg, J. M., Brucato, J. R., & Colangeli, L. 2001, *A&A*, 367, 355
 Mirabel, I. F., Lutz, D., & Maza, J. 1991, *A&A*, 243, 367
 Moorwood, A. F. M. 1986, *A&A*, 166, 4
 Mouri, H., Kawara, K., Taniguchi, Y., & Nishida, M. 1990, *ApJ*, 356, L39
 Murakami, H., et al. 2007, *PASJ*, 59, 369
 Murakawa, K., Tamura, M., & Nagata, T. 2000, *ApJS*, 128, 603
 Nagar, N. M., Wilson, A. S., Falcke, H., Veilleux, S., & Maiolino, R. 2003, *A&A*, 409, 115
 Ohyama, Y., et al. 2007, *PASJ*, 59, 411
 Onaka, T., et al. 2007, *PASJ*, 59, 401
 Pendleton, Y. J., Sandford, S. A., Allamandola, L. J., Tielens, A. G. G. M., & Sellgren, K. 1994, *ApJ*, 437, 683
 Perez-Gonzalez, P. G., et al. 2005, *ApJ*, 630, 82
 Rawlings, M. G., Adamson, A. J., & Whittet, D. C. B. 2003, *MNRAS*, 341, 1121
 Rieke, G. H., & Lebofsky, M. J. 1985, *ApJ*, 288, 618
 Risaliti, G., et al. 2003, *ApJ*, 595, L17
 Risaliti, G., et al. 2006, *MNRAS*, 365, 303
 Sanders, D. B., & Mirabel, I. F. 1996, *ARA&A*, 34, 749
 Sanders, D. B., Soifer, B. T., Elias, J. H., Madore, B. F., Matthews, K., Neugebauer, G., & Scoville, N. Z. 1988a, *ApJ*, 325, 74
 Sanders, D. B., Soifer, B. T., Elias, J. H., Neugebauer, G., & Matthews, K. 1988b, *ApJ*, 328, L35
 Sani, E., et al. 2008, *ApJ*, 675, 96
 Shirahata, M., et al. 2008, in preparation
 Smith, R. G., Sellgren K., & Tokunaga, A. T. 1989, *ApJ*, 344, 413
 Smith, R. G., Sellgren, K., & Brooke, T. Y. 1993, *MNRAS*, 263, 749
 Soifer, B. T., Sanders, D. B., Madore, B. F., Neugebauer, G., Danielson, G. E., Elias, J. H., Lonsdale, C. J., & Rice, W. L. 1987, *ApJ*, 320, 238
 Soifer, B. T. et al. 2000, *AJ*, 119, 509
 Soifer, B. T. et al. 2001, *AJ*, 122, 1213
 Spoon, H. W. W., Keane, J. V., Tielens, A. G. G. M., Lutz, D., & Moorwood, A. F. M. 2001, *A&A*, 365, L353

- Spoon, H. W. W., et al. 2004, ApJS, 154, 184
- Tanaka, M., Sato, S., Nagata, T., & Yamamoto, T. 1990, ApJ, 352, 724
- Tokunaga A. T., Sellgren K., Smith R. G., Nagata T., Sakata A., Nakada Y., 1991, ApJ, 380, 452
- Tokunaga, A. T. 2000, in Allen's Astrophysical Quantities, ed. A. N. Cox (4th ed; Berlin: Springer), 143
- Veilleux, S., Kim, D. -C., & Sanders, D. B. 1999, ApJ, 522, 113
- Veilleux, S., Kim, D. -C., Sanders, D. B., Mazzarella, J. M., & Soifer, B. T. 1995, ApJS, 98, 171
- Voit, G. M. 1992, MNRAS, 258, 841
- Whittet, D. C. B., Bode, M. F., Longmore, A. J., Adamson, A. J., McFadzean, A. D., Aitken, D. K., & Roche, P. F. 1988, MNRAS, 233, 321
- Wynn-Williams, C. G. 1984, in Galactic and Extragalactic Infrared Spectroscopy, ed. M. F. Kessler, and J. P. Phillips (D. Reidel Publishing Company), 133

Table 1. ULIRGs observed with the AKARI IRC and their *IRAS*-based infrared emission properties

Object	Redshift	f_{12} (Jy)	f_{25} (Jy)	f_{60} (Jy)	f_{100} (Jy)	$\log L_{\text{IR}}$ (L_{\odot})	f_{25}/f_{60}	Optical Class	Remark
(1)	(2)	(3)	(4)	(5)	(6)	(7)	(8)	(9)	(10)
IRAS 03521+0028	0.152	<0.11	0.20	2.52	3.62	12.5	0.08 (C)	LINER	$z > 0.15$
IRAS 04074-2801	0.153	<0.07	0.07	1.33	1.72	12.2	0.05 (C)	LINER	
IRAS 05020-2941	0.154	<0.06	0.10	1.93	2.06	12.3	0.05 (C)	LINER	
IRAS 09463+8141	0.156	<0.07	<0.07	1.43	2.29	12.3	<0.05 (C)	LINER	
IRAS 10091+4704	0.246	<0.06	<0.08	1.18	1.55	12.6	<0.07 (C)	LINER	
IRAS 11028+3130	0.199	<0.09	0.09	1.02	1.44	12.4	0.09 (C)	LINER	
IRAS 11180+1623	0.166	<0.08	<0.19	1.19	1.60	12.2	<0.16 (C)	LINER	
IRAS 14121-0126	0.151	0.06	0.11	1.39	2.07	12.3	0.08 (C)	LINER	
IRAS 16333+4630	0.191	<0.06	0.06	1.19	2.09	12.4	0.05 (C)	LINER	
IRAS 21477+0502	0.171	<0.09	0.16	1.14	1.46	12.3	0.14 (C)	LINER	
IRAS 23129+2548	0.179	<0.08	0.08	1.81	1.64	12.4	0.04 (C)	LINER	
IRAS 01199-2307	0.156	<0.11	<0.16	1.61	1.37	12.3	<0.1 (C)	HII-region	$z > 0.15$
IRAS 01355-1814	0.192	<0.06	0.12	1.40	1.74	12.4	0.09 (C)	HII-region	
IRAS 03209-0806	0.166	<0.10	<0.13	1.00	1.69	12.2	<0.13 (C)	HII-region	
IRAS 10594+3818	0.158	<0.09	<0.15	1.29	1.89	12.2	<0.12 (C)	HII-region	
IRAS 12447+3721	0.158	<0.12	0.10	1.04	0.84	12.1	0.10 (C)	HII-region	
IRAS 13469+5833	0.158	<0.05	0.04	1.27	1.73	12.2	0.03 (C)	HII-region	
IRAS 14202+2615	0.159	0.18	0.15	1.49	1.99	12.4	0.10 (C)	HII-region	
IRAS 15043+5754	0.151	<0.12	0.07	1.02	1.50	12.1	0.07 (C)	HII-region	
IRAS 17068+4027	0.179	<0.08	0.12	1.33	1.41	12.3	0.09 (C)	HII-region	
IRAS 22088-1831	0.170	<0.09	0.07	1.73	1.73	12.4	0.04 (C)	HII-region	
IRAS 00482-2721	0.129	<0.10	<0.18	1.13	1.84	12.0	<0.16 (C)	LINER	$z < 0.15$
IRAS 08572+3915	0.058	0.32	1.70	7.43	4.59	12.1	0.23 (W)	LINER	
IRAS 09539+0857	0.129	<0.15	<0.15	1.44	1.04	12.0	<0.11 (C)	LINER	
IRAS 10494+4424	0.092	<0.12	0.16	3.53	5.41	12.2	0.05 (C)	LINER	
IRAS 16468+5200	0.150	<0.06	0.10	1.01	1.04	12.1	0.10 (C)	LINER	
IRAS 16487+5447	0.104	<0.07	0.20	2.88	3.07	12.1	0.07 (C)	LINER	
IRAS 17028+5817	0.106	<0.06	0.10	2.43	3.91	12.1	0.04 (C)	LINER ^a	
IRAS 17044+6720	0.135	<0.07	0.36	1.28	0.98	12.1	0.28 (W)	LINER	
IRAS 00456-2904	0.110	<0.08	0.14	2.60	3.38	12.2	0.05 (C)	HII-region	$z < 0.15$
IRAS 01298-0744	0.136	<0.12	0.19	2.47	2.08	12.3	0.08 (C)	HII-region	
IRAS 01569-2939	0.141	<0.11	0.14	1.73	1.51	12.2	0.08 (C)	HII-region	
IRAS 11387+4116	0.149	0.12	<0.14	1.02	1.51	12.2	<0.14 (C)	HII-region	
IRAS 13539+2920	0.108	<0.09	0.12	1.83	2.73	12.0	0.07 (C)	HII-region	
IRAS 01494-1845	0.158	<0.08	<0.15	1.29	1.85	12.2	<0.12 (C)	unclassified	
IRAS 02480-3745	0.165	<0.05	<0.11	1.25	1.49	12.2	<0.09 (C)	unclassified	
IRAS 04313-1649	0.268	<0.07	0.07	1.01	1.10	12.6	0.07 (C)	unclassified	
IRAS 08591+5248	0.158	<0.10	<0.16	1.01	1.53	12.2	<0.16 (C)	unclassified	
IRAS 10035+2740	0.165	<0.14	<0.17	1.14	1.63	12.3	<0.15 (C)	unclassified	
IRAS 05189-2524	0.042	0.73	3.44	13.67	11.36	12.1	0.25 (W)	Seyfert 2	
IRAS 14394+5332	0.105	0.03	0.35	1.95	2.39	12.1	0.18 (C)	Seyfert 2	
IRAS 17179+5444	0.147	<0.08	0.20	1.36	1.91	12.2	0.15 (C)	Seyfert 2	
IRAS 23498+2423	0.212	<0.10	0.12	1.02	1.45	12.5	0.12 (C)	Seyfert 2	
UGC 5101	0.040	0.25	1.03	11.54	20.23	12.0	0.09 (C)	LINER	interesting
IRAS 19254-7245	0.062	0.22	1.24	5.48	5.79	12.1	0.23 (W)	Seyfert 2	

Notes.

Col.(1): Object name.

Col.(2): Redshift.

Cols.(3)–(6): f_{12} , f_{25} , f_{60} , and f_{100} are *IRAS* fluxes at $12\mu\text{m}$, $25\mu\text{m}$, $60\mu\text{m}$, and $100\mu\text{m}$, respectively, taken from Kim & Sanders (1998), except UGC 5101 and IRAS 19254–7245, for which *IRAS FSC* fluxes are shown.

Col.(7): Decimal logarithm of infrared (8–1000 μm) luminosity in units of solar luminosity (L_{\odot}), calculated with $L_{\text{IR}} = 2.1 \times 10^{39} \times D(\text{Mpc})^2 \times (13.48 \times f_{12} + 5.16 \times f_{25} + 2.58 \times f_{60} + f_{100})$ ergs s^{-1} (Sanders & Mirabel 1996). Since the calculation is based on our adopted cosmology, the infrared luminosities differ slightly (<10%) from the values shown in Kim & Sanders (1998, their Table 1, column 15). For sources that have upper limits in some *IRAS* bands, we can derive upper and lower limits on the infrared luminosity by assuming that the actual flux is the *IRAS*-upper limit and zero value, respectively. The difference between the upper and lower values is usually very small, less than 0.2 dex. We assume that the infrared luminosity is the average of these values.

Col.(8): *IRAS* 25 μm to 60 μm flux ratio. ULIRGs with $f_{25}/f_{60} < 0.2$ and > 0.2 are classified as cool and warm sources (denoted as “C” and “W”), respectively (Sanders et al. 1988b).

Col.(9): Optical spectral classification by Veilleux et al. (1999), except UGC 5101 and IRAS 19254–7245. For UGC 5101 and IRAS 19254–7245, optical classification is based on Veilleux et al. (1995) and Mirabel et al. (1991), respectively.

Col.(10): Remarks on individual objects.

^a: IRAS 17028+5817 consists of western (W) and eastern (E) nuclei. IRAS 17028+5817 W and E are classified optically as a LINER and HII-region, respectively (Veilleux et al. 1999). The optical classification of the combined spectrum of both nuclei is a LINER (Veilleux et al. 1999; their Table 2).

Table 2. Observation log of the AKARI IRC

Object (1)	Observation ID (2)	Observation date (3)
IRAS 03521+0028	1100200-001	2007 August 19
IRAS 04074-2801	1100201-001	2007 August 14
IRAS 05020-2941	1100003-001	2007 February 28
IRAS 09463+8141	1100004-001	2006 October 8
IRAS 10091+4704	1100122-001	2007 May 7
IRAS 11028+3130	1100006-001	2006 November 26
IRAS 11180+1623	1100202-001	2007 June 5
IRAS 14121-0126	1100011-001	2007 January 22
IRAS 16333+4630	1100013-001	2007 February 8
IRAS 21477+0502	1100207-001	2007 May 22
IRAS 23129+2548	1100015-001	2006 December 22
IRAS 01199-2307	1100209-001	2007 July 1
IRAS 01355-1814	1100018-001	2007 January 6
IRAS 03209-0806	1100210-001	2007 August 8
IRAS 10594+3818	1100021-001	2006 November 23
IRAS 12447+3721	1100022-001	2006 December 15
IRAS 13469+5833	1100023-001	2006 December 7
IRAS 14202+2615	1100212-001	2007 July 15
IRAS 15043+5754	1100213-001	2007 June 23
IRAS 17068+4027	1100026-001	2007 February 26
IRAS 22088-1831	1100214-001	2007 May 19
IRAS 00482-2721	1100036-001	2006 December 21
IRAS 08572+3915	1100049-001	2006 October 29
IRAS 09539+0857	1100267-001	2007 May 19
IRAS 10494+4424	1100266-001	2007 May 16
IRAS 16468+5200	1100249-001	2007 August 10
IRAS 16487+5447	1100247-001	2007 August 6
IRAS 17028+5817	1100248-001	2007 August 8
IRAS 17044+6720	1100297-001	2007 May 31
IRAS 00456-2904	1100221-001	2007 June 19
IRAS 01298-0744	1100226-001	2007 July 10
IRAS 01569-2939	1100225-001	2007 July 7
IRAS 11387+4116	1100269-001	2007 May 29
IRAS 13539+2920	1100235-001	2007 July 6
IRAS 01494-1845	1100215-001	2007 July 10
IRAS 02480-3745	1100030-001	2007 January 14
IRAS 04313-1649	1100031-001	2007 February 22
IRAS 08591+5248	1100121-001	2007 April 21
IRAS 10035+2740	1100216-001	2007 May 15
IRAS 05189-2524	1100129-001	2007 March 8
IRAS 14394+5332	1100283-001	2007 June 25
IRAS 17179+5444	1100253-001	2007 August 23
IRAS 23498+2423	1100287-001	2007 July 1
UGC 5101	1100134-001	2007 April 22
IRAS 19254-7245	1100132-001	2007 March 30

Notes.

Col.(1): Object name.

Col.(2): Observation ID.

Col.(3): Observation date in UT.

Table 3. Properties of 3.3 μm PAH emission, derived from AKARI IRC spectra

Object	$f_{3.3\text{PAH}}$ ($\times 10^{-14}$ ergs s^{-1} cm^{-2})	$L_{3.3\text{PAH}}$ ($\times 10^{41}$ ergs s^{-1})	$L_{3.3\text{PAH}}/L_{\text{IR}}$ ($\times 10^{-3}$)	rest $\text{EW}_{3.3\text{PAH}}$ (nm)
(1)	(2)	(3)	(4)	(5)
IRAS 03521+0028	2.2	12.2	0.1	108
IRAS 04074–2801	0.9	5.0	0.1	37
IRAS 05020–2941	1.0	5.5	0.07	53
IRAS 09463+8141	2.2	12.6	0.2	149
IRAS 10091+4704	0.7	11.4	0.08	75
IRAS 11028+3130	0.6	6.3	0.07	100
IRAS 11180+1623	0.5	3.1	0.05	36
IRAS 14121–0126	2.9	15.4	0.2	80
IRAS 16333+4630	2.1	19.0	0.2	63
IRAS 21477+0502	0.6	4.0	0.05	29
IRAS 23129+2548	<0.4	<2.5	<0.03	<12
IRAS 01199–2307	0.8	4.5	0.07	76
IRAS 01355–1814	0.6	5.2	0.05	54
IRAS 03209–0806	2.2	14.8	0.25	68
IRAS 10594+3818	2.6	15.4	0.25	79
IRAS 12447+3721	1.3	7.7	0.15	187
IRAS 13469+5833	1.4	8.1	0.15	40
IRAS 14202+2615	4.2	25.3	0.25	32
IRAS 15043+5754	2.0	10.9	0.2	95
IRAS 17068+4027	2.2	17.4	0.2	144
IRAS 22088–1831	<0.2	<1.3	<0.02	<8
IRAS 00482–2721	1.3	4.8	0.1	99
IRAS 08572+3915	<4.2	<2.9	<0.07	<5
IRAS 09539+0857	1.2	4.5	0.1	73
IRAS 10494+4424	3.6	6.7	0.1	55
IRAS 16468+5200	0.6	3.0	0.07	78
IRAS 16487+5447	3.3	8.0	0.15	90
IRAS 17028+5817W	3.3	8.3	0.15	82
IRAS 17044+6720	2.3	9.8	0.2	14
IRAS 00456–2904	4.0	10.9	0.2	56
IRAS 01298–0744	1.7	7.4	0.1	133
IRAS 01569–2939	1.8	8.4	0.15	84
IRAS 11387+4116	1.9	10.2	0.2	59
IRAS 13539+2920	4.3	11.2	0.3	52
IRAS 17028+5817E	0.4	1.1	0.02	34
IRAS 01494–1845	2.2	12.8	0.2	68
IRAS 02480–3745	1.5	9.9	0.15	265
IRAS 04313–1649	<0.4	<6.3	<0.05	<73
IRAS 08591+5248	1.4	8.4	0.15	39
IRAS 10035+2740	1.4	9.1	0.15	80
IRAS 05189–2524	30.0	10.7	0.2	10
IRAS 14394+5332	6.2	15.3	0.4	71
IRAS 17179+5444	1.2	5.9	0.1	16
IRAS 23498+2423	<1.9	<21	<0.25	<8
UGC 5101	22.5	7.3	0.2	33
IRAS 19254–7245	3.8	3.1	0.07	5

Col. (1): Object name. Col. (2): Observed flux of $3.3 \mu\text{m}$ PAH emission. Col. (3): Observed luminosity of $3.3 \mu\text{m}$ PAH emission. Col. (4): Observed $3.3 \mu\text{m}$ PAH-to-infrared luminosity ratio in units of 10^{-3} . Typical ratios for less infrared-luminous starbursts are $\sim 10^{-3}$ (Mouri et al. 1990; Imanishi 2002). Col. (5): Rest-frame equivalent width of $3.3 \mu\text{m}$ PAH emission. Those for starbursts are typically $\sim 100 \text{ nm}$ (Moorwood 1986; Imanishi & Dudley 2000).

Table 4. Optical depths of absorption features and AGN signatures, derived from AKARI IRC spectra

Object	Observed $\tau_{3.1}$	Observed $\tau_{3.4}$	A_V (mag)	AGN signatures	
				EW _{3.3PAH}	$\tau_{3.1}$ or $\tau_{3.4}$
(1)	(2)	(3)	(4)	(5)	(6)
IRAS 03521+0028	0.2	—	>3	—	—
IRAS 04074–2801	0.6	—	>10	○	○
IRAS 05020–2941	0.5	—	>8	—	○
IRAS 09463+8141	0.5	—	>8	—	○
IRAS 10091+4704	—	—	—	—	—
IRAS 11028+3130	0.6	—	>10	—	○
IRAS 11180+1623	0.7	—	>11	○	○
IRAS 14121–0126	1.0	—	>16	—	○
IRAS 16333+4630	2.0	—	>33	—	○
IRAS 21477+0502	—	—	—	○	—
IRAS 23129+2548	—	—	—	○	—
IRAS 01199–2307	0.8	—	>13	—	○
IRAS 01355–1814	1.0	—	>16	—	○
IRAS 03209–0806	0.3	—	>5	—	—
IRAS 10594+3818	0.4	—	>6	—	—
IRAS 12447+3721	—	—	—	—	—
IRAS 13469+5833	0.2	—	>3	—	—
IRAS 14202+2615	—	—	—	○	—
IRAS 15043+5754	0.4	—	>6	—	—
IRAS 17068+4027	1.5	—	>25	—	○
IRAS 22088–1831	0.5	—	>8	○	○
IRAS 00482–2721	1.0	—	>16	—	○
IRAS 08572+3915	0.3	0.8	119–205	○	○
IRAS 09539+0857	1.1	—	>18	—	○
IRAS 10494+4424	0.8	—	>13	—	○
IRAS 16468+5200	1.0	—	>16	—	○
IRAS 16487+5447	—	—	—	—	—
IRAS 17028+5817W	0.9	—	>15	—	○
IRAS 17044+6720	—	0.15	21–38	○	—
IRAS 00456–2904	0.4	—	>6	—	—
IRAS 01298–0744	—	—	—	—	—
IRAS 01569–2939	—	—	—	—	—
IRAS 11387+4116	0.5	—	>8	—	○
IRAS 13539+2920	0.2	—	>3	—	—
IRAS 17028+5817E	—	—	—	○	—
IRAS 01494–1845	0.7	—	>11	—	○
IRAS 02480–3745	—	—	—	—	—
IRAS 04313–1649	—	—	—	—	—
IRAS 08591+5248	0.3	—	>5	○	—
IRAS 10035+2740	0.3	—	>5	—	—
IRAS 05189–2524	—	—	—	○	—
IRAS 14394+5332	—	—	—	—	—
IRAS 17179+5444	—	—	—	○	—
IRAS 23498+2423	—	—	—	○	—
UGC 5101	1.0	0.6	102–166	○	○
IRAS 19254–7245	0.2	0.5	74–128	○	○

Col. (1): Object name. Col. (2): Observed optical depth of 3.1 μm absorption features due to ice-covered dust grains. Col. (3): Observed optical depth of 3.4 μm absorption features due to bare carbonaceous dust grains. Col. (4): Dust extinction (A_V) toward the 3–4 μm continuum emission regions, derived from the absorption optical depths, assuming the Galactic dust extinction curve and a foreground screen dust distribution model. For those with detected 3.1 μm absorption, but no measurable $\tau_{3.4}$ values, the derived A_V values should be taken as lower limits (see text in §5.4). Col. (6): Signatures of an AGN, based on the low value of the rest-frame equivalent width of the 3.3 μm PAH emission. \odot : present. Col. (7): Signatures of an AGN, based on the large optical depth of the 3.1 μm and/or 3.4 μm absorption features. \odot : present.

Table 5. Observed ULIRGs with ground-based telescopes and observation log

Object	Redshift	Spectral type	Date	Telescope	Integration	P.A. ⁴		Standard Stars		
(1)	(2)	(3)	(4)	(5)	(6)	(7)	(8)	(9)	(10)	(11)
IRAS 00482–2721	0.129	LINER	2007 September 25	Keck NIRSPEC	32	0	HR 173	4.6	G3V	5800
IRAS 04103–2838	0.118	LINER	2007 September 24	Keck NIRSPEC	48	0	HR 1179	5.2	F8V	6000
IRAS 00456–2904	0.110	HII	2006 July 19	Subaru IRCS	38	90	HR 210	4.0	G3V	5800
IRAS 22491–1808	0.076	HII	2006 July 18	Subaru IRCS	60	110	HR 8544	5.1	G2V	5830
IRAS 01004–2237	0.118	HII	2007 September 24	Keck NIRSPEC	48	15	HR 173	4.6	G3V	5800
IRAS 02021–2013	0.116	Unclassified	2007 January 15	Subaru IRCS	32	90	HR 695	3.7	G0V	5930
IRAS 23233+2817	0.114	Sy2	2007 September 25	Keck NIRSPEC	40	–16	HR 8792	4.9	F7V	6240
IRAS 23389+0300	0.145	Sy2	2007 September 25	Keck NIRSPEC	64	10	HR 8931	5.1	F8V	6000

Notes:

Col.(1): Object name. Col.(2): Redshift. Col.(3): Optical spectral classification by Veilleux et al. (1999). Col.(4): Observation date in UT. Col.(5): Telescope and instrument. Col.(6): Net on-source integration time in minutes. Col.(7): Position angle of the slit. Col.(8): Standard star name. Col.(9): Adopted L -band magnitude. Col.(10): Stellar spectral type. Col.(11): Effective temperature.

^a: 0° corresponds to the north-south direction. Position angle increases counterclockwise on the sky plane.

Table 6. Properties of $3.3 \mu\text{m}$ PAH emission for ULIRGs observed with ground-based telescopes

Object	$f_{3.3\text{PAH}}$ ($\times 10^{-14} \text{ ergs s}^{-1} \text{ cm}^{-2}$)	$L_{3.3\text{PAH}}$ ($\times 10^{41} \text{ ergs s}^{-1}$)	rest $\text{EW}_{3.3\text{PAH}}$ (nm)
(1)	(2)	(3)	(4)
IRAS 00482–2721	0.9	3.6	115
IRAS 04103–2838	3.3	10.2	45
IRAS 00456–2904	1.8	4.8	125
IRAS 22491–1808	3.5	4.3	180
IRAS 01004–2237	1.6	5.1	30
IRAS 02021–2013	1.4	4.4	55
IRAS 23233+2817	1.7	4.9	30
IRAS 23389+0300	2.3	11.1	90

Notes.

Col.(1): Object name. Col.(2): Observed flux of $3.3 \mu\text{m}$ PAH emission. Col.(3): Observed luminosity of $3.3 \mu\text{m}$ PAH emission. Col.(4): Rest-frame equivalent width of $3.3 \mu\text{m}$ PAH emission.

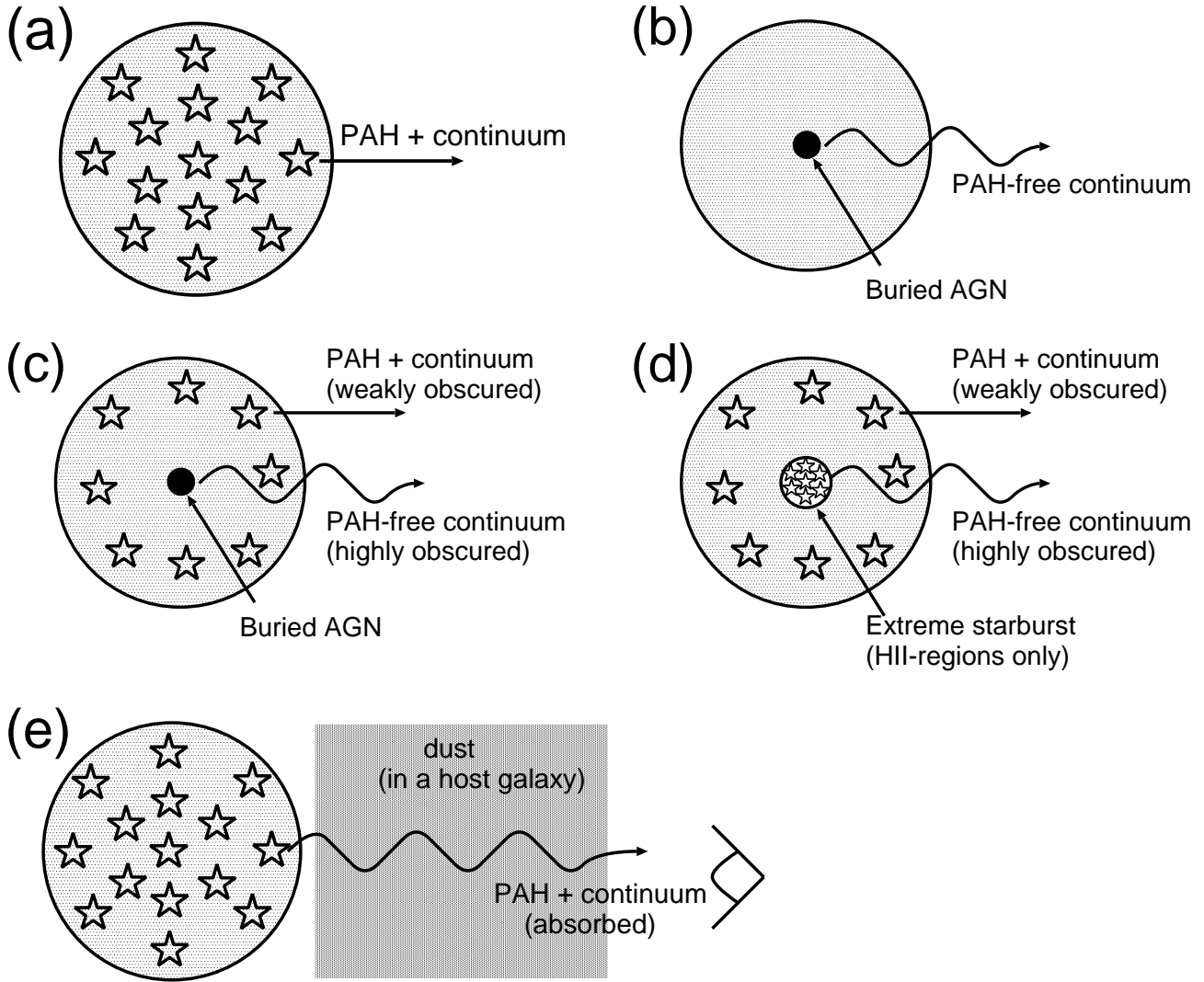
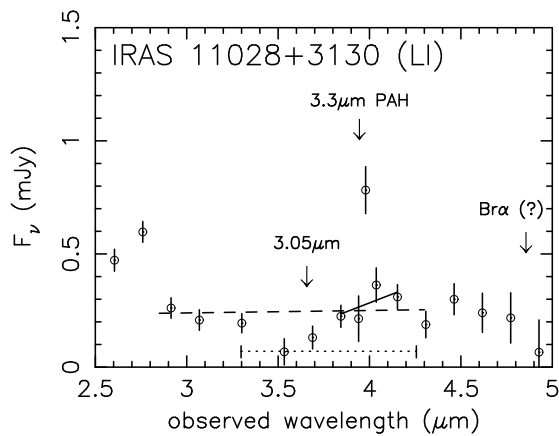
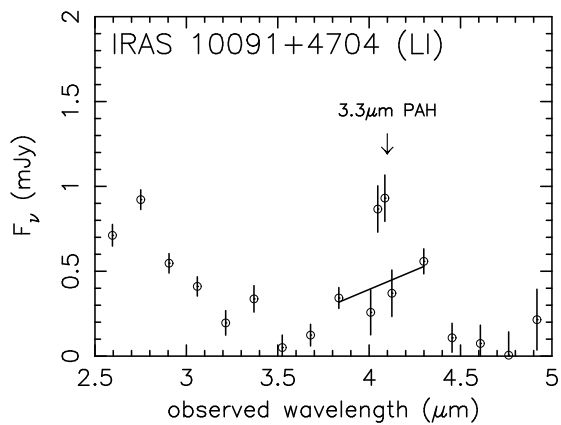
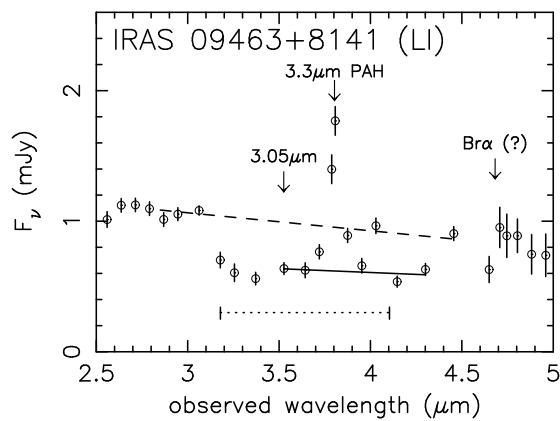
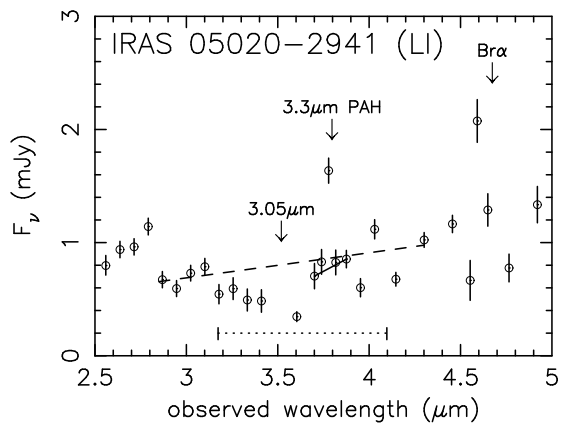
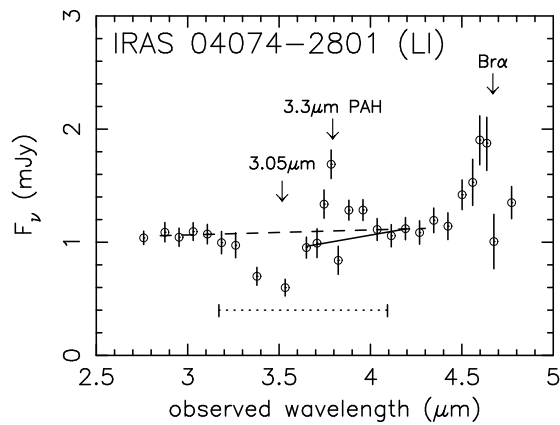
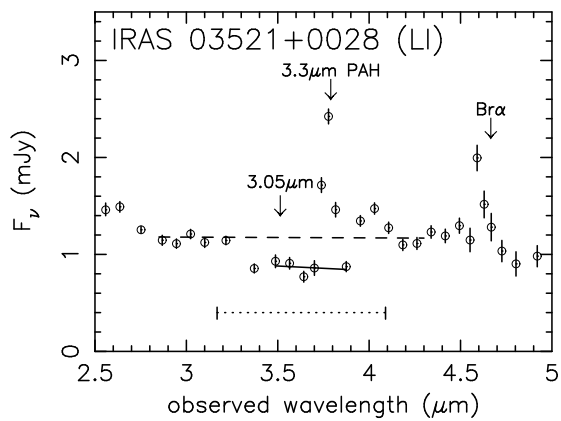
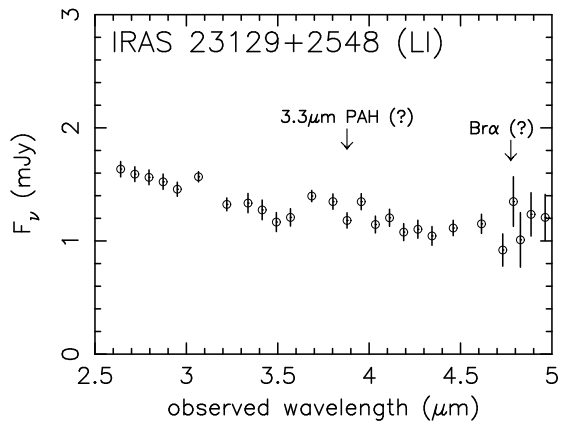
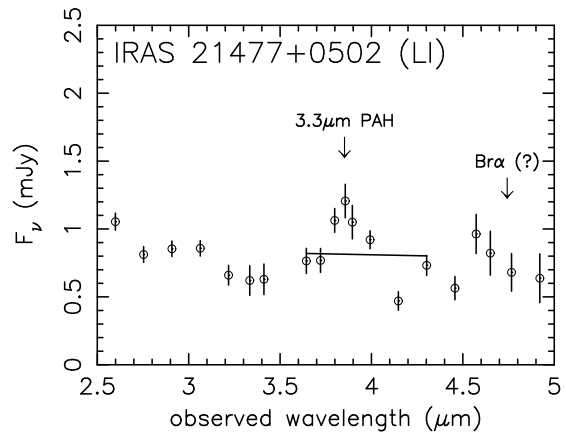
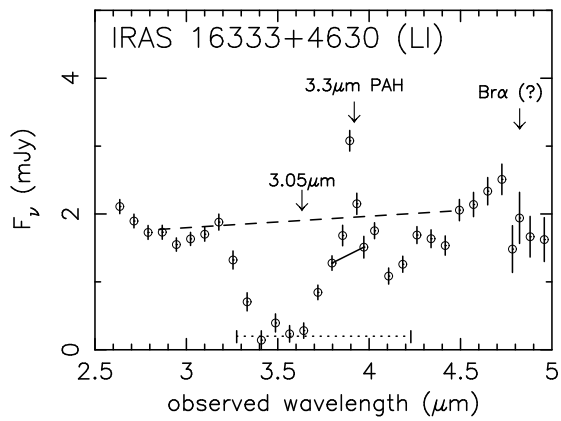
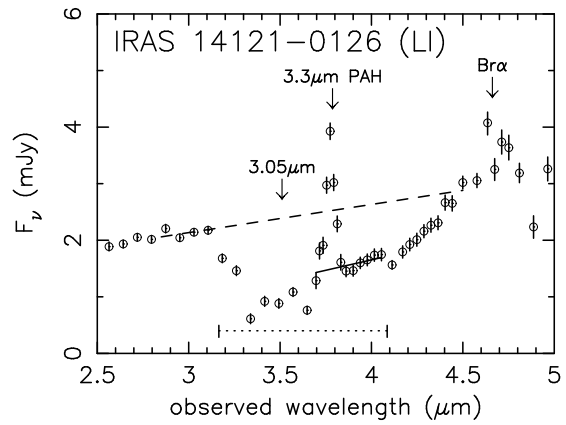
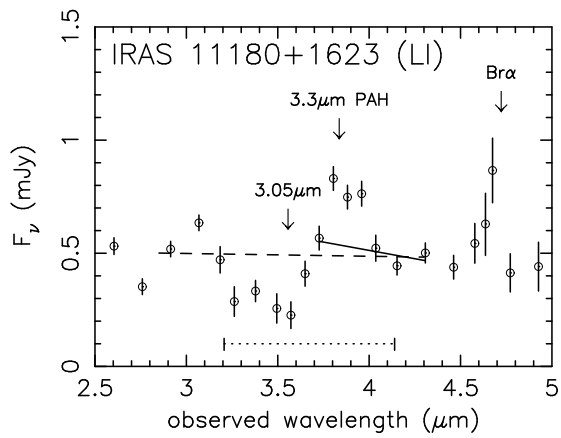
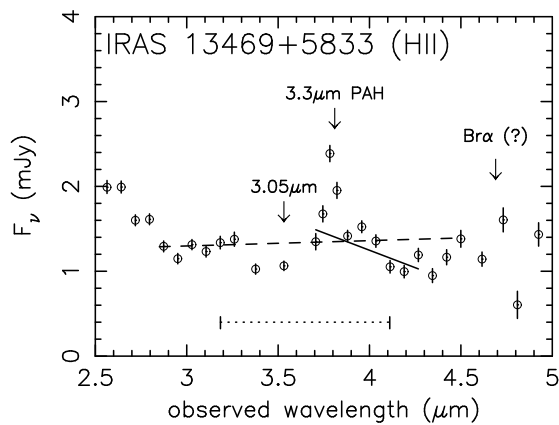
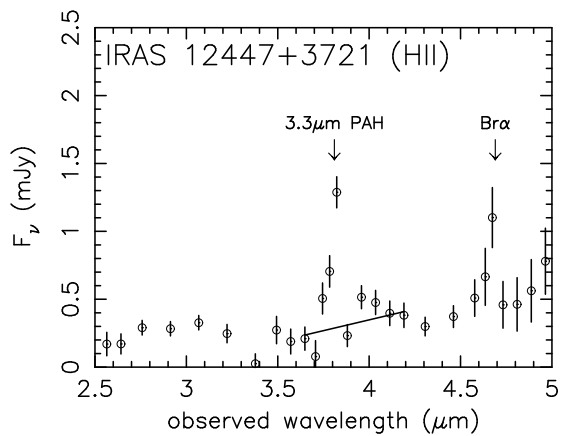
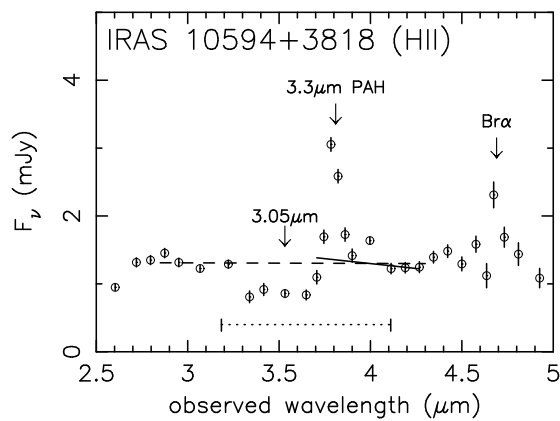
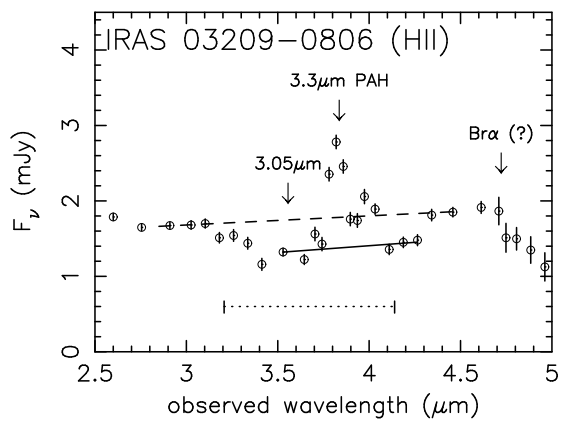
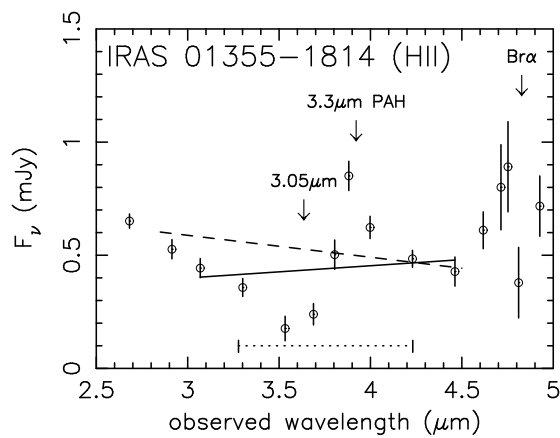
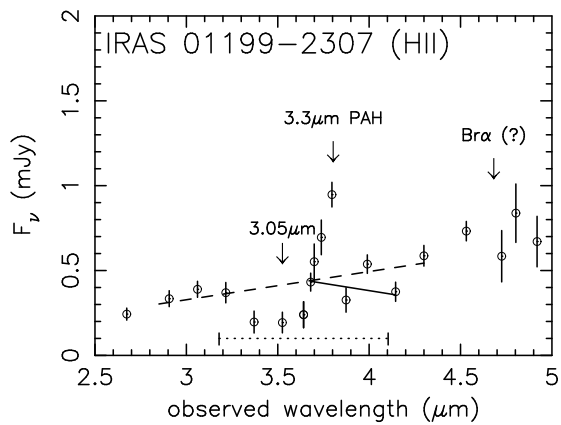
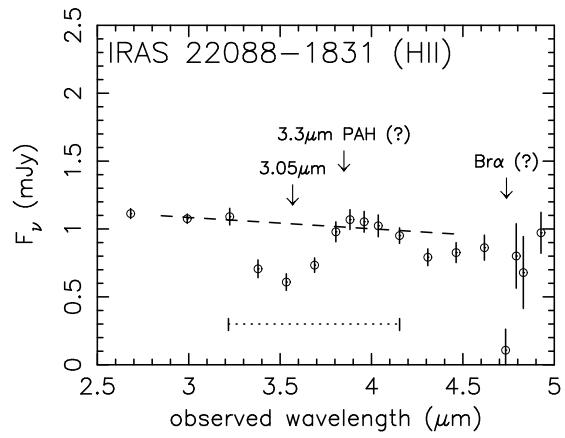
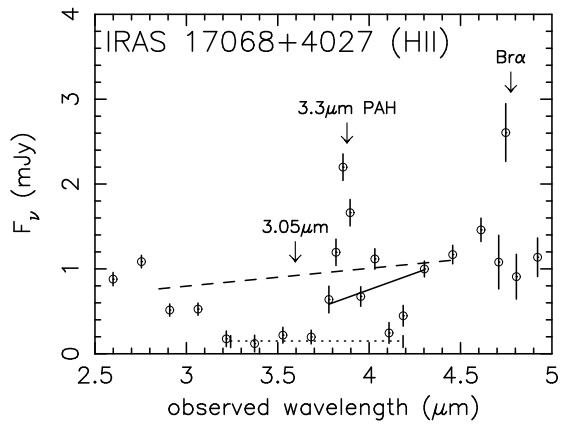
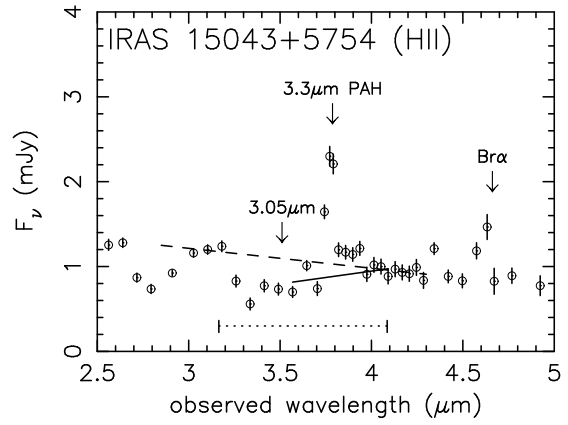
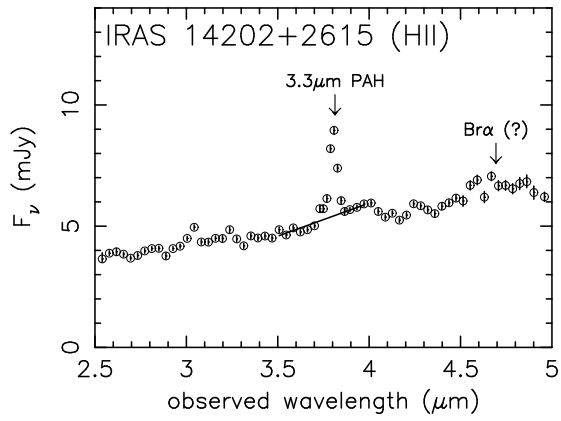


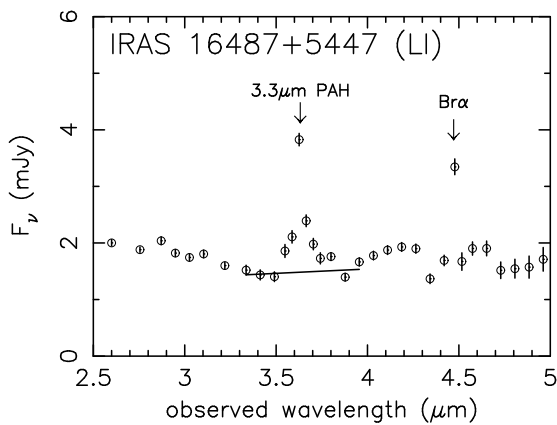
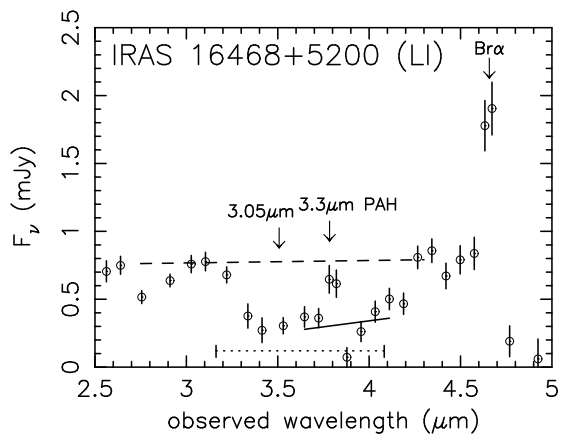
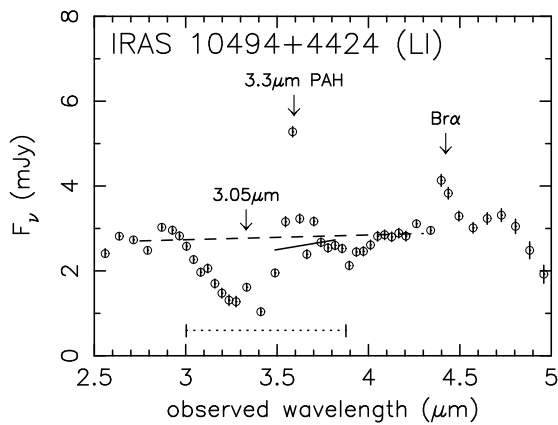
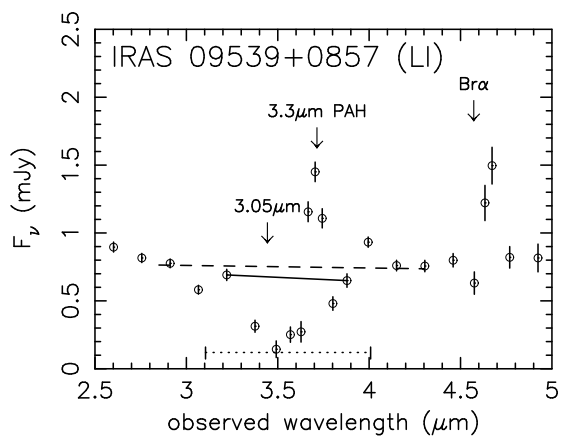
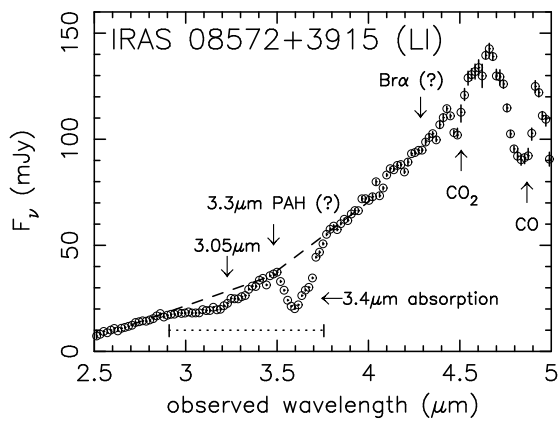
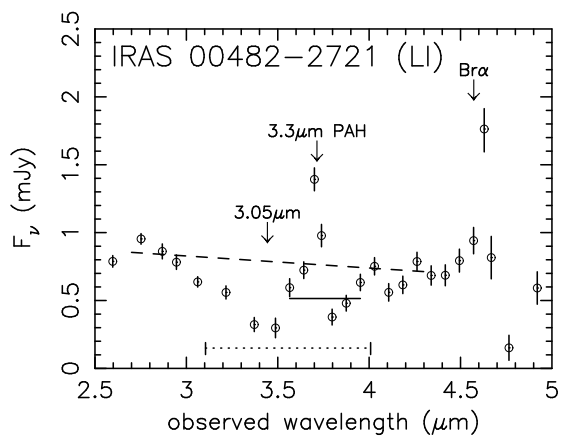
Fig. 1. (a): Geometry of energy sources and dust in a normal starburst. The open star symbols indicate “stars” in a starburst. The energy sources (stars) and dust are spatially well mixed. Large equivalent width PAH emission is observed, regardless of the amount of dust extinction, because both PAH and continuum emission fluxes are similarly attenuated in this geometry. (b): Geometry of the energy source and dust in a buried AGN. The energy source (a compact mass-accreting supermassive black hole) is more centrally concentrated than the surrounding dust. No PAH emission is observed, because PAHs are destroyed by strong X-ray radiation from the AGN (Voit 1992). (c): A buried AGN and starburst composite. The starburst surrounds the central buried AGN. The observed spectrum is a superposition of PAH + continuum emission from the starburst and PAH-free continuum from the AGN. Since the buried AGN is more highly obscured than the surrounding starbursts, the starburst emission generally makes a strong contribution to the observed flux even if the starburst is energetically insignificant. (d): An exceptionally centrally concentrated extreme starburst whose emitting volume is predominantly occupied by HII-regions, without photodissociation regions and molecular gas. Such an extreme starburst produces no PAH emission, similar to a buried AGN. (e): A normal starburst nucleus (mixed dust/source geometry) obscured by a large amount of foreground dust in an edge-on host galaxy, exterior to the ULIRG’s nuclear core. This geometry can produce a strong dust absorption feature whose optical depth is larger than the maximum threshold obtained in the mixed dust/source geometry.

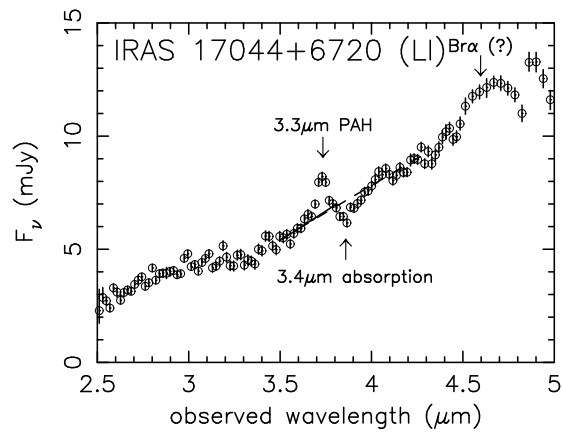
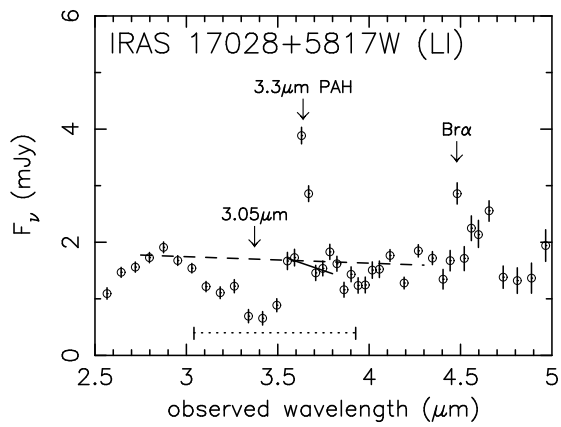


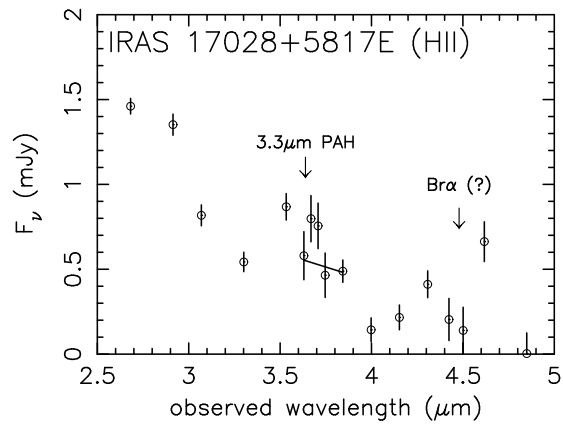
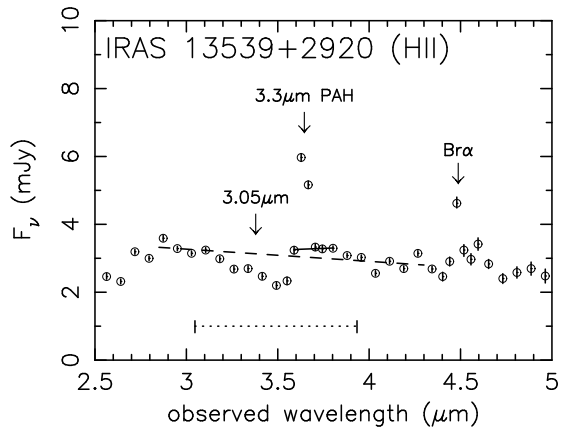
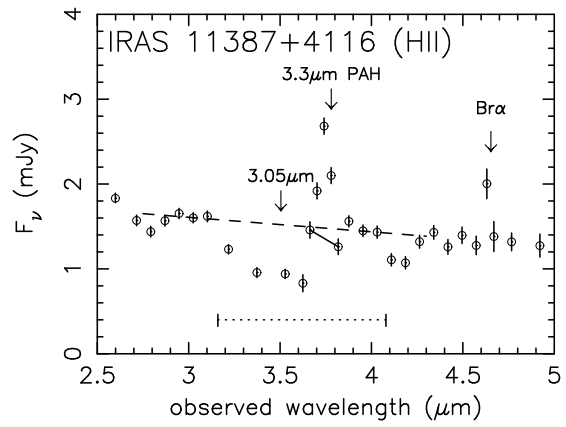
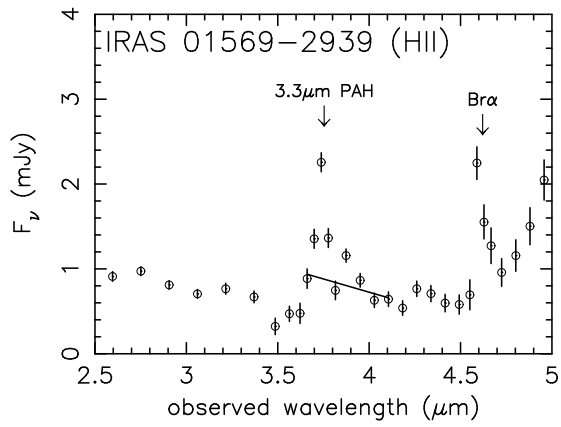
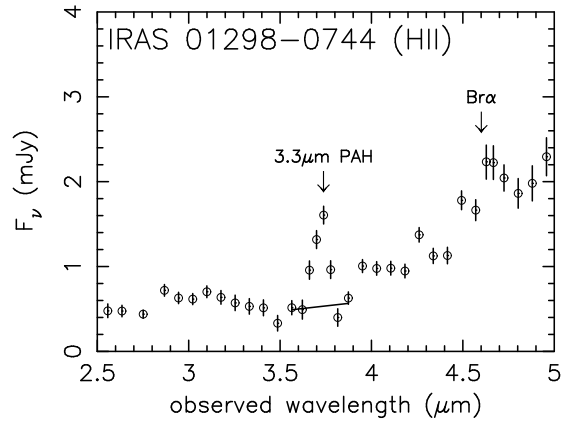
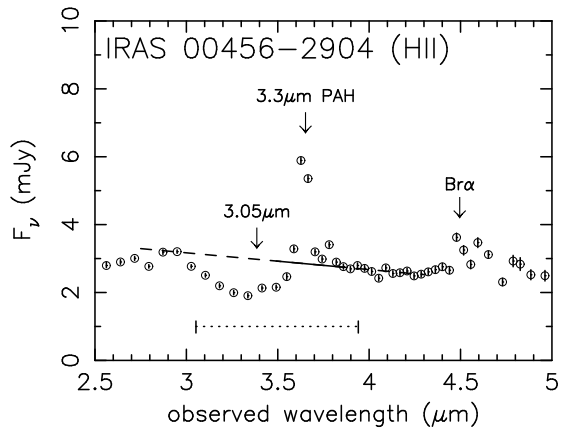


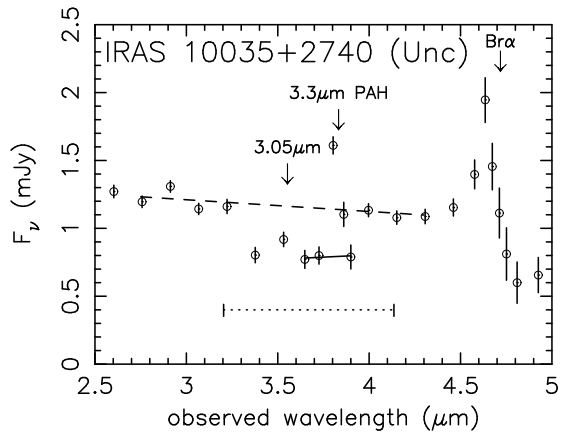
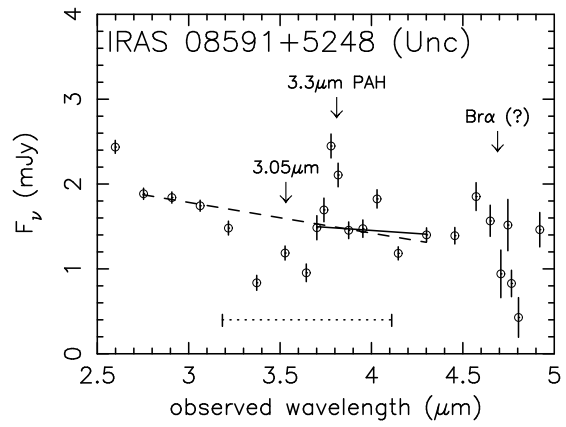
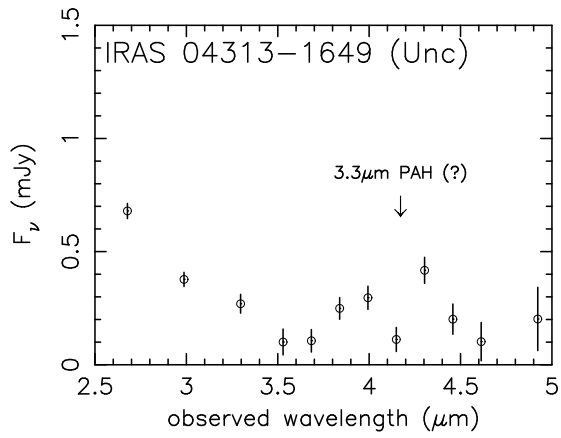
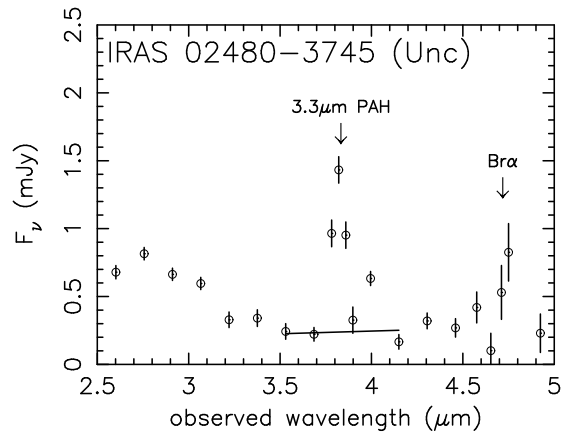
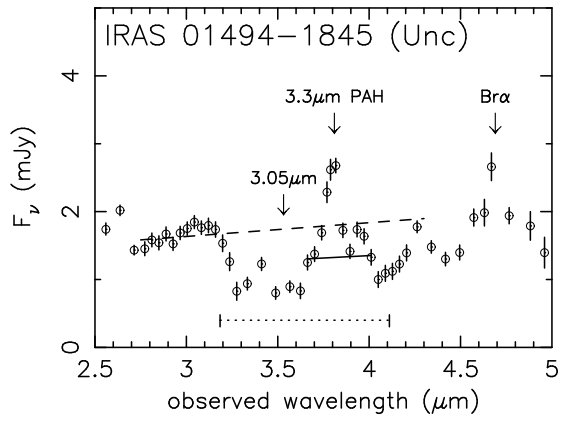


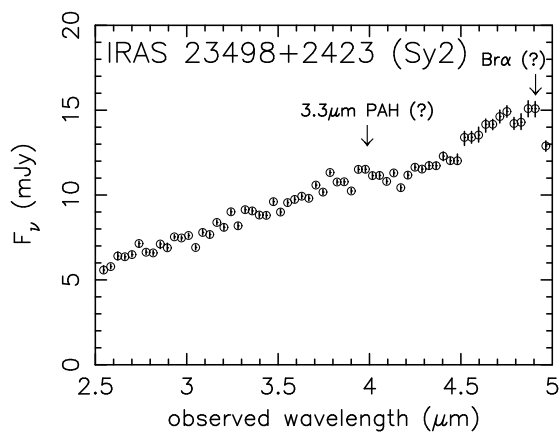
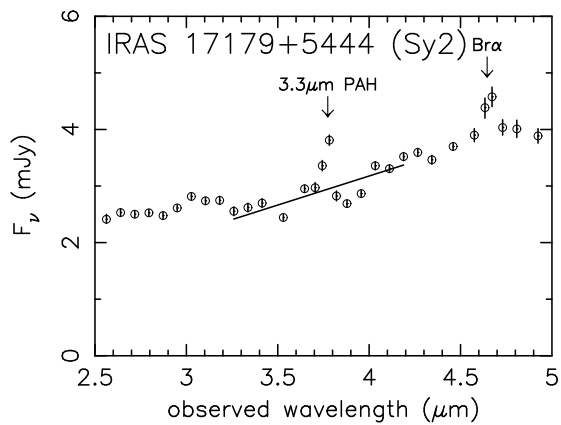
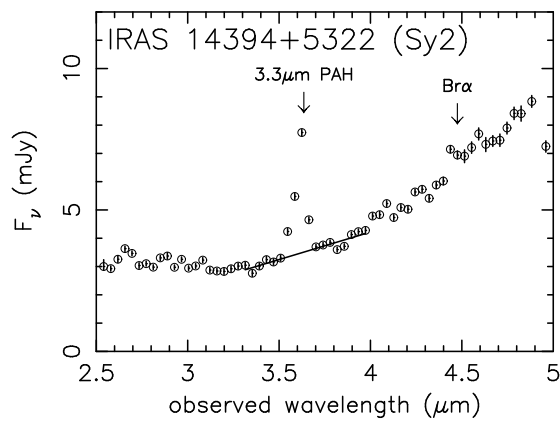
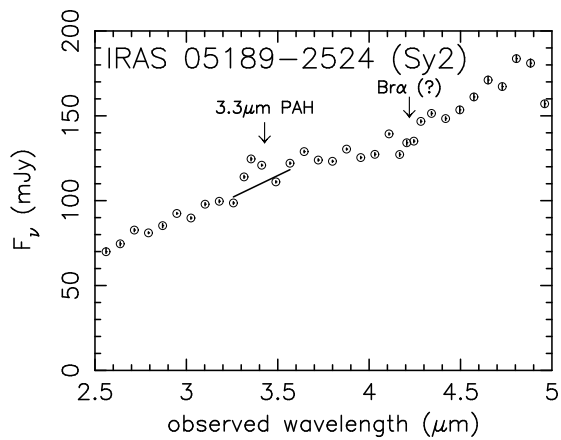












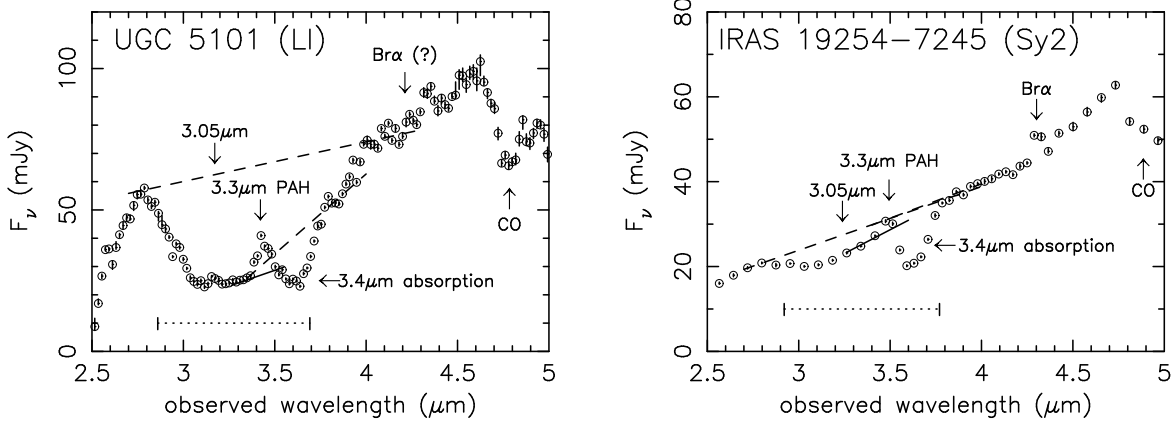


Fig. 2. AKARI IRC 2.5–5.0 μm spectra of ULIRGs. The order of objects is the same as shown in Table 1, except IRAS 17028+5817E, whose spectrum is shown in the group of HII-region ULIRGs. “LI”, “HII”, “Unc”, and “Sy2” indicate optically LINER, HII-region, unclassified, and Seyfert 2 ULIRGs, respectively. The abscissa and ordinate are the observed wavelength in μm and F_ν in mJy, respectively. The lower arrows with “3.3 μm PAH” indicate the expected wavelength of the 3.3 μm PAH emission ($\lambda_{\text{rest}} = 3.29 \mu\text{m}$). The solid lines are the adopted continua used to estimate the 3.3 μm PAH emission fluxes for PAH-detected sources. The arrows with “3.05 μm ” or “3.4 μm ” denote the 3.1 μm ice-covered and 3.4 μm bare carbonaceous dust absorption features, respectively. Regarding ULIRGs with clear signatures for these absorption features, dashed straight lines are plotted to show the adopted continuum levels used to estimate the absorption optical depths. The dotted lines indicate the wavelength range in which effects of the broad 3.1 μm ice absorption feature can be significant ($\lambda_{\text{rest}} = 2.75\text{--}3.55 \mu\text{m}$, adopted from the spectrum of Elias 16; Smith et al. 1989). The ice absorption feature is usually very strong at $\lambda_{\text{rest}} = 2.9\text{--}3.2 \mu\text{m}$, but the profiles and wavelength range of weaker absorption wings are found to vary among different Galactic objects (Smith et al. 1989). Br α emission is also indicated. “CO” or “CO₂” denote CO and CO₂ absorption features, respectively.

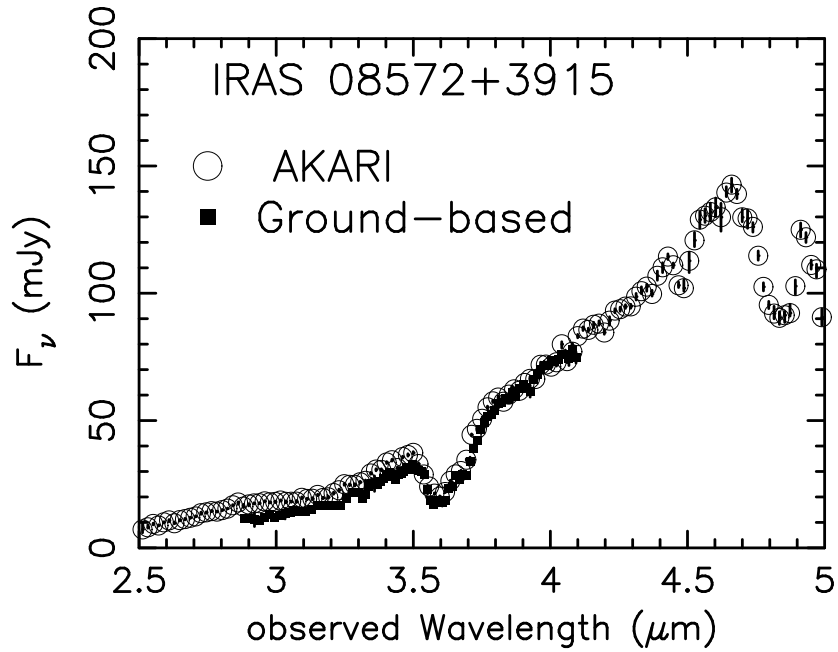


Fig. 3. Comparison of the AKARI IRC slitless spectrum of IRAS 08572+3915 (open circles) with ground-based 1.6-arcsecond wide slit spectrum taken with IRTF SpeX (filled squares) (Imanishi et al. 2006a). The seeing size at the time of the IRTF observations was 0.6–0.7 arcseconds in the K -band (2–2.5 μm). The ordinate of the IRTF SpeX spectrum is converted from F_λ in $\text{W m}^{-2} \mu\text{m}^{-1}$ to F_ν in mJy. Both spectra have similar spectral shapes and flux levels. Statistical 1σ errors are shown as vertical lines, but are too small to discern at $\lambda_{\text{obs}} < 4.5 \mu\text{m}$. A slight discrepancy at the shorter wavelength could be explained by a non-negligible contribution from extended stellar emission in the host galaxy (see §4 for more details).

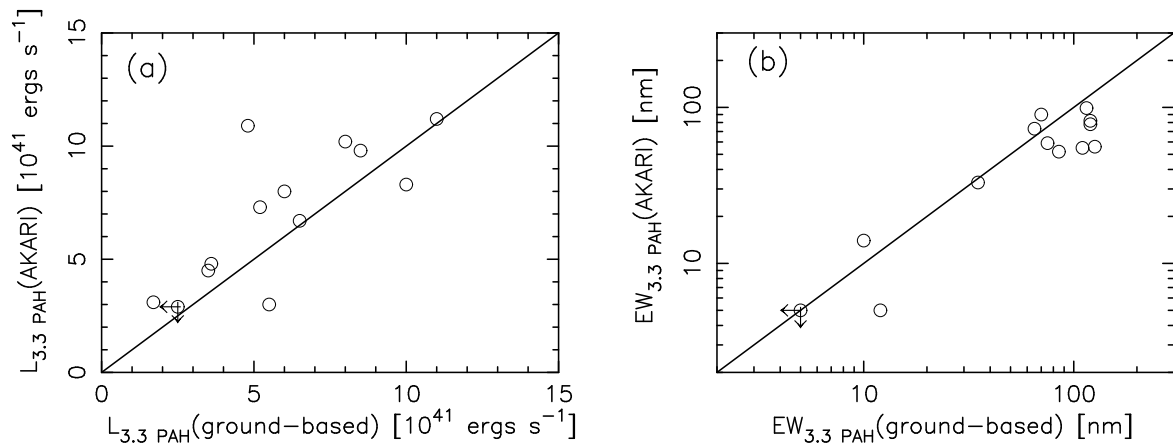


Fig. 4. (a) : Comparison of the 3.3 μm PAH luminosity measured with ground-based slit spectra (abscissa) and AKARI IRC slitless spectra (ordinate) for ULIRGs for which both AKARI and ground-based spectra at 3–4 μm are available. These ULIRGs are IRAS 00482–2721, 08572+3915, 09539+0857, 10494+4424, 16468+5200, 16487+5447, 17028+5817W, 17044+6720, 00456–2904, 11387+4116, 13539+2920, UGC 5101, and IRAS 19254–7245 (Imanishi & Maloney 2003; Risaliti et al. 2003; Imanishi et al. 2006a; this paper). All ULIRGs are at $z < 0.15$. (b) : Comparison of rest-frame 3.3 μm PAH equivalent width measured with ground-based slit spectra (abscissa) and AKARI IRC slitless spectra (ordinate) for the same ULIRGs.

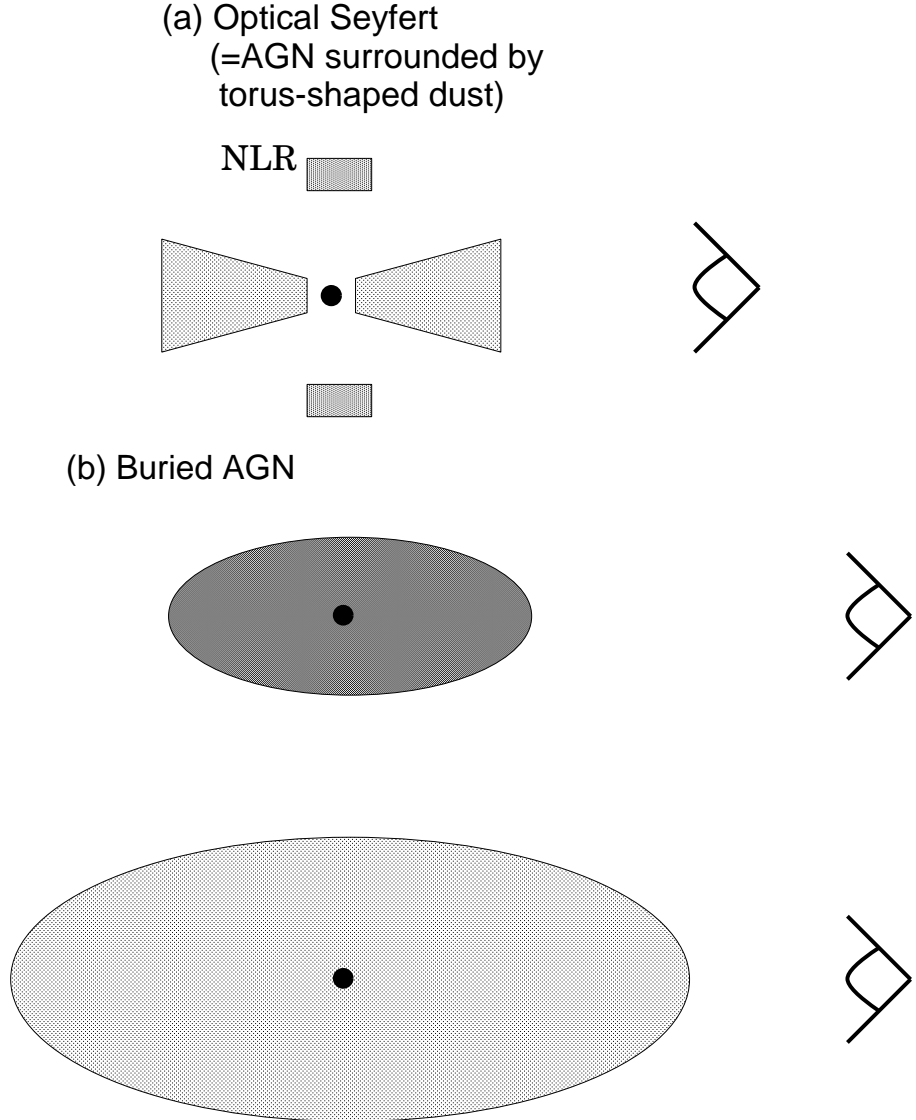


Fig. 5. Schematic diagram of nuclear dust distribution. (a): An AGN classified optically as a Seyfert. The small filled circle at the center represents the central mass-accreting supermassive black hole. When we look from the right side, the AGN is classified as a Seyfert 2. As the dust has angular momentum, dust distribution is axisymmetrical. When the total amount of nuclear dust is modest, dust along the direction of the lowest dust column density can be transparent to the AGN’s ionizing radiation, producing the so-called narrow line regions (NLRs), photoionized by the AGN’s radiation, above a torus scale height. In this case, dust distribution can be approximated as torus-shaped. Optical emission line ratios from NLRs are classified as Seyfert 2s, which are different from normal starburst galaxies. (b): A buried AGN classified optically as a non-Seyfert. Dust surrounds the central AGN along virtually all lines-of-sight. Since the total amount of nuclear dust is larger than that of a Seyfert-type AGN, even the direction of the lowest dust column density can be opaque to the AGN’s radiation, and dust column density along our line-of-sight is generally larger than a Seyfert 2 AGN (see §5.7). The darker shade indicates higher dust volume density. The larger amount of total nuclear dust in a buried AGN compared to a Seyfert 2 AGN can originate either in a higher dust volume density with a similar volume (upper case), a larger volume of nuclear obscuring dust with similar volume density (lower case), or both larger volume and higher volume density of nuclear dust.

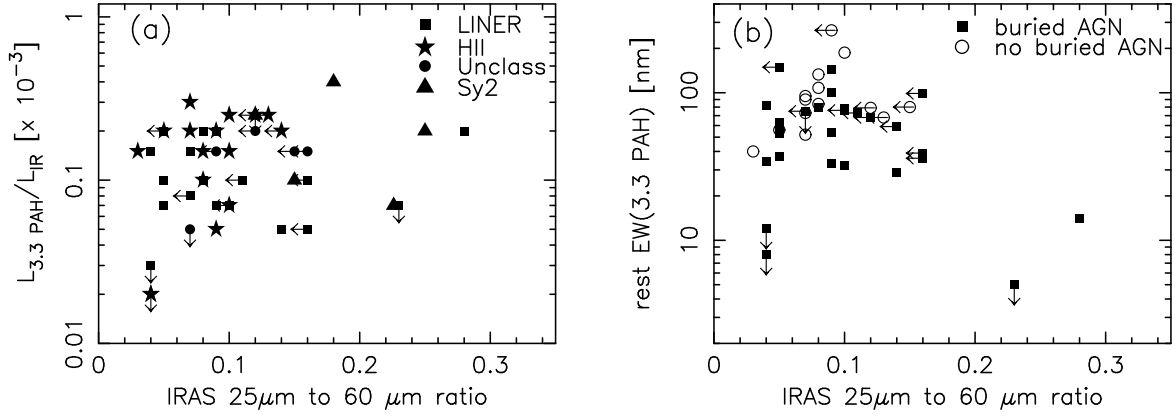
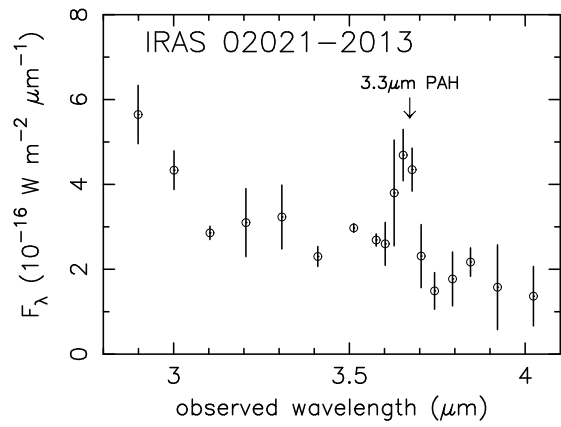
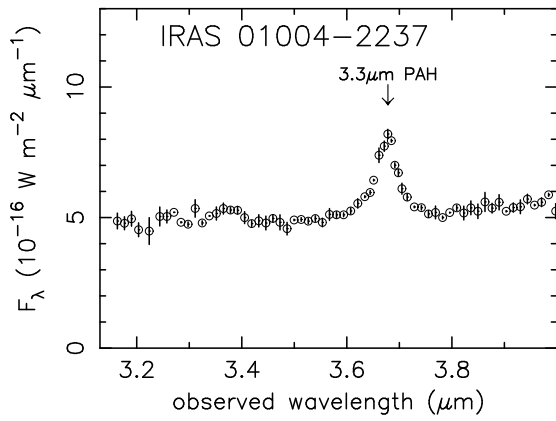
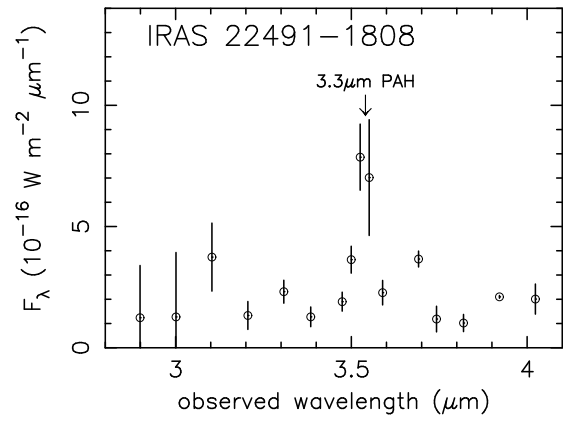
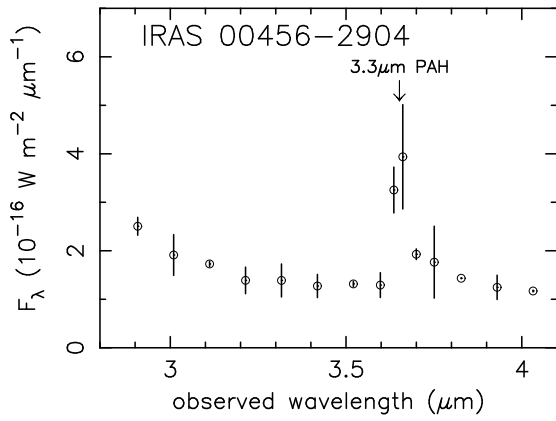
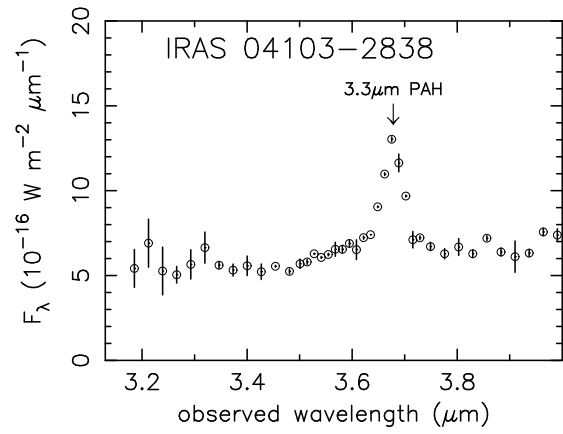
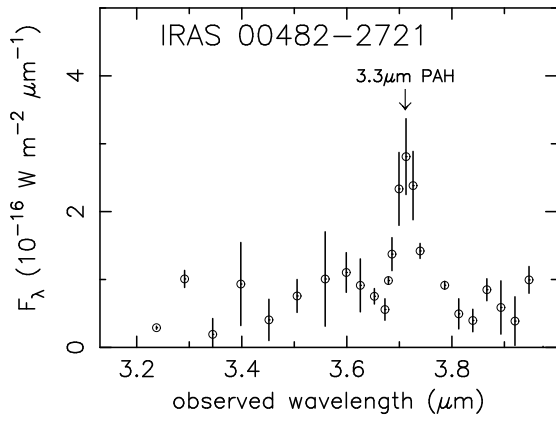


Fig. 6. (a): *IRAS* 25 μm -to-60 μm flux ratio (abscissa) and observed 3.3 μm PAH to infrared luminosity ratio (ordinate). Filled squares: LINER ULIRGs. Filled stars: HII-region ULIRGs. Filled circles: Optically unclassified ULIRGs. Filled triangles: Seyfert 2 ULIRGs. The two ULIRGs of interest, UGC 5101 and IRAS 19254–7245, are classified as LINER and Seyfert 2, respectively. For IRAS 17028+5817, emission from double nuclei is resolved in AKARI IRC spectra, but not in the *IRAS* data. For this source, we assume that both nuclei have the same far-infrared colors as measured with *IRAS*. (b): *IRAS* 25 μm -to-60 μm flux ratio (abscissa) and rest frame equivalent widths of the 3.3 μm PAH emission (ordinate) for non-Seyfert ULIRGs. Filled squares: ULIRGs with buried AGN signatures. Open circles: ULIRGs with no obvious buried AGN signatures in the AKARI IRC 2.5–5 μm spectra.



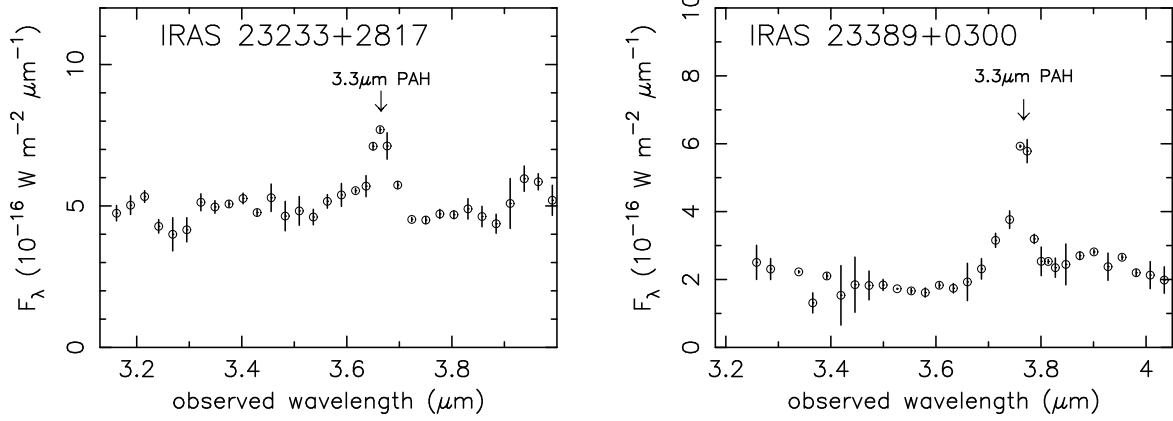


Fig. 7. Ground-based infrared L -band ($2.8\text{--}4.1\ \mu\text{m}$) spectra of the observed ULIRGs. The abscissa is the observed wavelength in μm , and the ordinate is F_λ in $10^{-16}\ \text{W m}^{-2}\ \mu\text{m}^{-1}$, following previously shown ground-based L -band spectra (Imanishi et al. 2006a; Imanishi 2006). The lower arrows with “ $3.3\ \mu\text{m}$ PAH” indicate the expected wavelength of the $3.3\ \mu\text{m}$ PAH emission ($\lambda_{\text{rest}} = 3.29\ \mu\text{m}$).